Acta Pharmaceutica Sinica B 2025;15(3):1211−1229

Chinese Pharmaceutical Association
Institute of Materia Medica, Chinese Academy of Medical Sciences

Acta Pharmaceutica Sinica B

www.elsevier.com/locate/apsb
www.sciencedirect.com

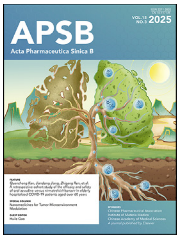

ORIGINAL ARTICLE

Intravenous delivery of STING agonists using acid-sensitive polycationic polymer-modified lipid nanoparticles for enhanced tumor immunotherapy

Ying He[a,†], Ke Zheng[c,†], Xifeng Qin[a], Siyu Wang[a], Xuejing Li[a], Huiwen Liu[d], Mingyang Liu[a], Ruizhe Xu[a], Shaojun Peng[b,*], Zhiqing Pang[a,*]

[a]*School of Pharmacy, Fudan University, Key Laboratory of Smart Drug Delivery, Ministry of Education, Shanghai 201203, China*
[b]*Guangdong Provincial Key Laboratory of Tumor Interventional Diagnosis and Treatment, Zhuhai People's Hospital (Zhuhai Hospital Affiliated with Jinan University), Zhuhai 519000, China*
[c]*School of Materials Science and Engineering, Dongguan University of Technology, Dongguan 523808, China*
[d]*Institute of Hematology, Union Hospital, Tongji Medical College, Huazhong University of Science & Technology, Wuhan 430022, China*

Received 1 March 2024; received in revised form 20 May 2024; accepted 22 May 2024

KEY WORDS

Polycationic polymer;
Lipid nanoparticles (LNP);
Cyclic dinucleotides;
ADU-S100;
Intravenous delivery;
Cancer nanotechnology;
The stimulator of interferon genes (STING) pathway;

Abstract Although cancer immunotherapy has made great strides in the clinic, it is still hindered by the tumor immunosuppressive microenvironment (TIME). The stimulator of interferon genes (STING) pathway which can modulate TIME effectively has emerged as a promising therapeutic recently. However, the delivery of most STING agonists, specifically cyclic dinucleotides (CDNs), is performed intratumorally due to their insufficient pharmacological properties, such as weak permeability across cell membranes and vulnerability to nuclease degradation. To expand the clinical applicability of CDNs, a novel pH-sensitive polycationic polymer-modified lipid nanoparticle (LNP-B) system was developed for intravenous delivery of CDNs. LNP-B significantly extended the circulation of CDNs and enhanced the accumulation of CDNs within the tumor, spleen, and tumor-draining lymph nodes compared with free CDNs thereby triggering the STING pathway of dendritic cells and repolarizing pro-tumor macrophages. These events subsequently gave rise to potent anti-tumor immune reactions and substantial inhibition of

---

*Corresponding authors.

E-mail addresses: shaojunpeng@ext.jnu.edu.cn (Shaojun Peng), zqpang@fudan.edu.cn (Zhiqing Pang).

[†] These authors made equal contributions to this work.

Peer review under the responsibility of Chinese Pharmaceutical Association and Institute of Materia Medica, Chinese Academy of Medical Sciences.

https://doi.org/10.1016/j.apsb.2024.06.004

CT26 colon cells

tumors in CT26 colon cancer-bearing mouse models. In addition, due to the acid-sensitive property of the polycationic polymer, the delivery system of LNP-B was more biocompatible and safer compared with lipid nanoparticles formulated with an indissociable cationic DOTAP (LNP-D). These findings suggest that LNP-B has great potential in the intravenous delivery of CDNs for tumor immunotherapy.

1. Introduction

Despite the remarkable advancements in tumor immunotherapy for the treatment of cancer[1−7], it still encounters numerous challenges. One of the biggest hurdles facing tumor immunotherapy is the presence of the tumor immunosuppressive microenvironment (TIME), which can hinder the effectiveness of treatment[8,9]. It has been found that the therapeutic effect of tumor immunotherapy largely depends on the production of type I interferon (IFN)[10−12]. Therefore, the cyclic GMP-AMP synthase (cGAS)-stimulator of interferon genes (STING) pathway, which triggers the production of type I IFN, has emerged as a promising therapeutic target for modulating the TIME and enhancing anti-tumor immunity[13−17]. Many STING agonists, namely cyclic dinucleotides (CDNs) have shown powerful anti-tumor efficacy in extensive research[18−20]. Although plenty of STING agonists have shown promise in tumor immunotherapy, the inherent properties of CDNs, such as the negative charge, high water solubility, vulnerability to nuclease degradation, and polar surface area, render them unsuitable candidates for systemic administration *via* intravenous injection[21]. The intratumoral injection also poses certain limitations to the development and deployment of such drugs across various indications. This administration mode greatly limits the clinical value of CDNs for the treatment of deep tumors or metastatic tumors because of the operation difficulty of intratumoral injection in the body[22]. Therefore, it is of great practical value to develop novel strategies to deliver CDNs by intravenous injection for tumor immunotherapy.

Recently, many researchers have devised various nanoparticle systems to facilitate intravenous delivery of CDNs as well as to activate a stronger anti-tumor immune response[23,24]. For instance, cationic liposomes prepared using a weight ratio of soy phosphatidylcholine (soy-PC) to 1,2-dioleoyl-3-trimethylammonium-propane (DOTAP) of 100:1 demonstrated an encapsulation efficiency of about 43% for cyclic GMP−AMP (cGAMP) and stimulated both innate and adaptive immune responses against preexisting tumors in orthotopic and genetically engineered models of basal-like triple-negative breast cancer[25]. A polymersome platform improved the half-life of encapsulated cGAMP by 40-fold, allowing for sufficient accumulation of cGAMP in tumors and activation of the STING pathway in the TIME[26]. CD103^{+} dendritic cells (DCs)-targeted liposomal CDN formulations presented enhanced anti-tumor immune responses as well as reduced off-target toxicities[27]. Nanodiscs formed by the CDN−PEG−lipid conjugate exhibited high efficiency in penetrating tumors and showed robust anti-tumor efficacy[28]. These findings confirm the viability of nanoparticle systems for intravenous delivery of CDNs. In comparison to exosomes, lipid nanoparticles (LNP) demonstrate higher efficacy in encapsulating negatively charged nucleic acid drugs. Unlike positively charged liposomes, LNP provide superior protection against degradation for CDNs. Given these factors, LNP show great potential for intravenous delivery of CDNs. However, the development of LNP has encountered difficulties attributed to patent protections and concerns over the potential toxicity of cationic phospholipids or ionizable phospholipids, which serve as crucial components in LNP for loading nucleic acid drugs and facilitating their escape from lysosomes[29].

Herein, we developed a novel pH-sensitive polycationic polymer-modified lipid nanoparticle (LNP-B) system for tumor delivery of CDNs intravenously, using ADU-S100 as a model CDN (Scheme 1). A new polycationic polymer−lipid conjugate, termed DSPE-PCB^{+}, which is capable of undergoing degradation to form an electroneutral zwitterionic polymer−lipid conjugate under acidic conditions, was used to facilitate the creation of lipid nanoparticles with a remarkable drug loading capacity and an acceptable safety profile. Considering that Mn^{2+} is an activator of cGAS and can bind cGAMP to form nanoparticles[30,31], Mn^{2+} was included in LNP-B to form a stable nano-structure. The physicochemical properties such as the diameter, potential, stability, drug loading, and drug release of LNP-B were characterized. The cellular uptake behavior of LNP-B by immune cells including dendritic cells (DCs) and macrophages and the STING pathway activation effect of LNP-B were carefully investigated *in vitro*. Following a single intravenous administration, we probed into the efficacy and its associated immunological mechanisms through examination of immune cell variations in tumors, spleens, and tumor-draining lymph nodes (TDLN) of CT26-bearing mice models. Finally, a deep examination of LNP-B's safety was conducted. Collectively, it has been found that the LNP-B was uniform, stable, and acid-sensitive, exhibiting the capability to activate the STING pathway of DCs and repolarize macrophages *in vitro*. Additionally, a single intravenous injection of LNP-B could inhibit the growth of tumors, and promote the "cold" tumor microenvironment into the "hot" tumor microenvironment. Overall, LNP-B was both safe and efficacious in enhancing tumor immunotherapy.

2. Materials and methods

2.1. *Materials and animals*

1,2-Dioleoyl-*sn*-glycero-3-phosphocholine (DOPC), cholesterol, 1,2-dioleoyl-3-trimethylammonium-propane (DOTAP), and 1,2-distearoyl-*sn*-glycero-3-phosphoethanolamine-*N*-[methoxy(polyethylene-glycol)-2000] (DSPE-mPEG2k) were purchased from AVT Pharmaceutical Tech Co., Ltd. (Shanghai, China). ADU-S100 was obtained from MedChemExpress (Shanghai, China). Dulbecco's modified Eagle's medium (DMEM, MA0212) and RPMI 1640 (MA0546) were from Meilun Biotechnology Co., Ltd. (Dalian, China). KO525 or APC anti-mouse CD45, APC anti-mouse CD11c, PB450 anti-mouse CD11b, FITC anti-mouse

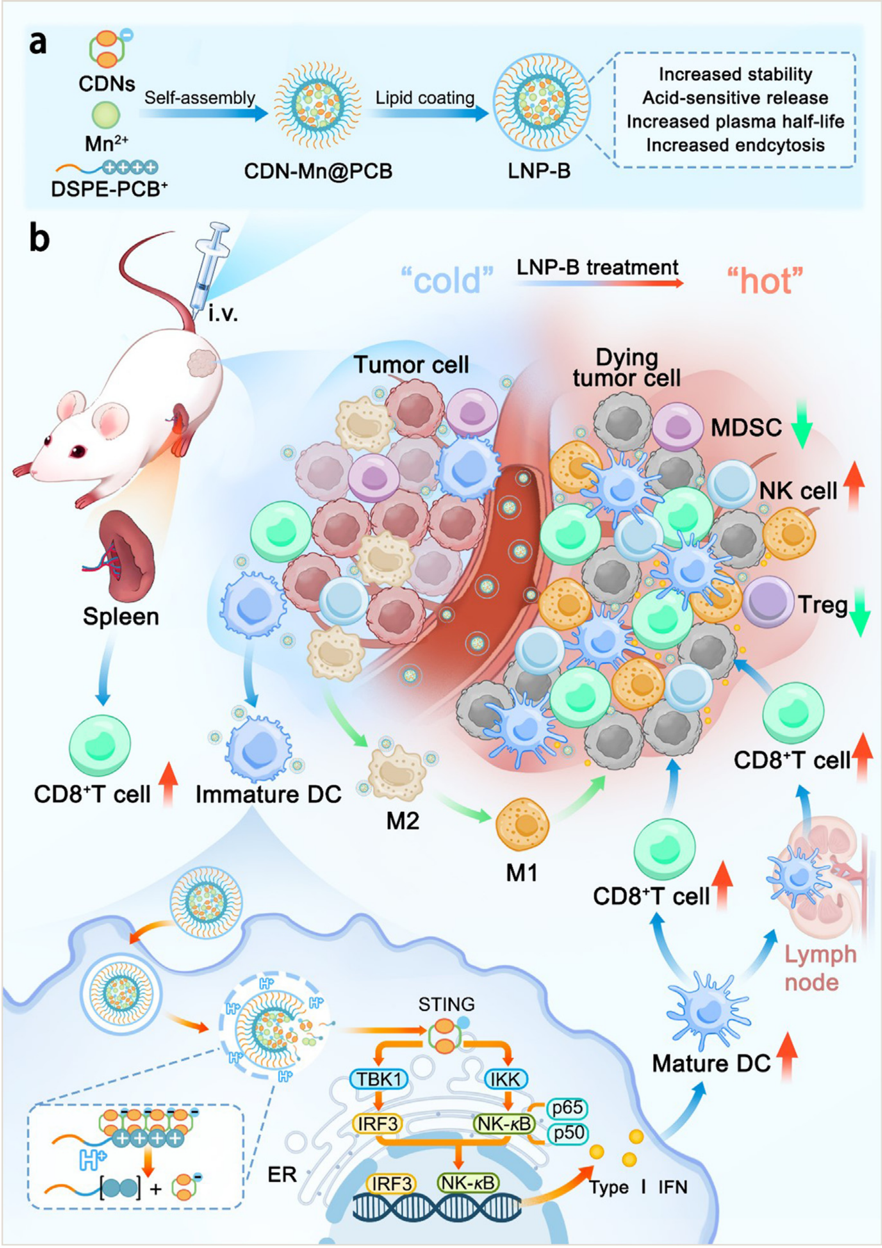

Scheme 1 Amplifying STING activation with LNP-B for cancer immunotherapy. **a**, LNP-B is composed of a core formed with CDNs, Mn^{2+}, a polycationic polymer-lipid DSPE-PCB^{+}, and a PEGylated lipid layer formed with DOPC, cholesterol, and DSPE-PEG. **b**, After being administered intravenously, LNP-B demonstrates a prolonged circulation time, allowing for enhanced accumulation within the tumor. Subsequently, LNP-B is internalized by immune cells such as DCs and transported to acidic lysosomes. Within this acidic environment, DSPE-PCB^{+} undergoes cleavage, resulting in the formation of the electroneutral zwitterionic-lipid DSPE-PCB. This cleavage disrupts the lipid nanoparticles and releases CDNs to activate the STING pathway, leading to reshaping the tumor immunosuppressive microenvironment and enhanced tumor immunotherapy.

CD11c, PE anti-mouse Ly6C, PE anti-mouse MHC-II, Alex 488 anti-mouse F4/80, PE anti-mouse CD49b, PerCP/Cy5 or APC anti-mouse CD3, FITC anti-mouse CD19, and Brilliant Violent 605 anti-mouse CD4 were purchased from Biolegend (San Diego, CA, USA). Cy5-conjugated 2'3'-cGAMP was obtained from Biolog Life Science Institute GmbH & Co. KG (Bremen, Germany). 2-(4-Amidinophenyl)-6-indolecarbamidine dihydrochloride (DAPI) was purchased from Beyotime (Nantong, China). Amiloride was obtained from Solarbio Life Sciences Co., Ltd. (Beijing, China). Recombinant murine macrophage colony stimulating factor (M-CSF) and granulocyte-macrophage colony-stimulating factor (GM-CSF) were from PeproTech (Cranbury, USA). phospho-NF-κB p65 (pS536), NF-κB p65, phospho-IRF3 (pS396), IRF3, phospho-TBK1 (pS172), TBK1, or β-actin and the relevant secondary antibodies (goat anti-rabbit IgG) were from Abcam (Shanghai, China). TNF-α and IFN-γ ELISA kits were obtained from MultiSciences Biotechnology Co., Ltd. (Hangzhou, China). IFN-β ELISA kit was acquired from Jianglai Biotechnology (Shanghai, China). Fetal bovine serum (FBS), penicillin streptomycin (P/S), and Trypsin-EDTA (0.25%) were from Gibco (Carlsbad, CA, USA). Deionized water was acquired from the Millipore Simplicity System (Bedford, MA, USA).

Murine colon cancer cell lines (CT26) were obtained from the Chinese Academy of Science Cells Bank (Shanghai, China). C57BL/6 and male BALB/c mice (6−8 weeks) were purchased from Lingchang Co., Ltd. (Shanghai, China). To create tumor-bearing mouse models, CT26 colon cancer cells (2×10^6) were transplanted into the lower right side of the back of male BALB/c mice. When the tumor volume reached around 200 mm^3, tumor-bearing mice were used for further experiments. All animal protocols and experiments were approved by the Animal Ethics Committee of Fudan University (2019-03-YJ-PZQ-01).

2.2. *Synthesis of LNP-B*

Firstly, DSPE-PCB^+ was synthesized by an atom transfer radical polymerization method (Supporting Information Schemes S1−S3)[32,33]. The molecular weight of DSPE-PCB^+ was 4900 Da determined by GPC. Details of the synthesis and characterization of DSPE-PCB^+ were given in Supporting Information. Secondly, to prepare the experimental components, in a typical synthesis process[30], manganese chloride methanol solution (100 mmol/L), CDNs methanol solution (1.45 mmol/L), and different concentrations of DSPE-PCB^+ methanol solutions with corresponding nitrogen-phosphorus (N/P) molar ratios of 2, 4, 6, and 12 were added to the Eppendorf tube respectively. The mixture was incubated on the rotary mixer for about 1 h, so that it could generate positively charged nanoparticle cores, called CDN-Mn@PCB-1, CDN-Mn@PCB-2, CDN-Mn@PCB-3, and CDN-Mn@PCB-4, respectively, through electrostatic interaction force and coordination bond. Afterward, the mixture was subjected to centrifugation at 20,000×*g* for 30 min (CP100NX, Hitachi, Japan) to remove unbounded CDNs and metal ions with methanol twice. Then, LNP-Bn ($n = 1, 2, 3$) was synthesized by mixing the screened CDN-Mn@PCB with a lipid ethanol solution containing DOPC, cholesterol, and DSPE-mPEG2k, and sonicating at 100 W in a sonication bath for 5 min followed by the addition of nuclease-free water until the ethanol concentration was 30% (*v*/*v*). To investigate the impact of cholesterol content on LNP-B, LNP-B1, LNP-B2, and LNP-B3 were produced with cholesterol and DOPC molar ratios of 0.5, 1, and 2, respectively, at a total lipid concentration of 26 mg/mL. Lastly, LNP-B was acquired by evaporating the organic solvent under reduced pressure and subsequently washed with PBS through centrifugal ultrafiltration with a molecular weight cutoff (MWCO) of 100 kDa. LNP-D was synthesized using the same method except for the replacement of DSPE-PCB^+ with DOTAP at equal moles of positive charges.

2.3. *Characterization of LNP-B*

The size and zeta potential of the CDN-Mn@PCB, LNP-B, and LNP-D were measured using a Zetasizer (Malvern, UK). The morphology of LNP-B was observed by a transmission electron microscope TEM (JEOL JEM-2010, Tokyo, Japan) after staining with 2% phosphotungstic acid. The encapsulation efficiency and loading capability of ADU-S100 in the CDN-Mn@PCB, LNP-B, and LNP-D were quantified by a high-performance liquid chromatography (Agilent 1260 Infinity II, Santa Clara, USA) method[34]. The encapsulation efficiency and loading capability of Mn^{2+} in the LNP-B and LNP-D were quantified by inductively coupled plasma-mass spectrometry (ICP-MS)[30].

The stability of LNP in PBS was monitored by measuring the particle size of LNP-B and LNP-D which were diluted to the same concentration with PBS and stored at 4°C. To assess the stability of LNP in FBS, LNP-B or LNP-D was incubated with 50% FBS at 37°C[35]. At specific time points (1, 4, 8, 12, and 24 h), 100 μL of samples were taken. The OD560 value of the samples was measured using a microplate reader (Bio-Tek Synergy H1, Santa Clara, USA). A 50% FBS solution without the addition of nanoparticles served as a control.

2.4. *In vitro drug release of LNP-B*

In vitro drug release of LNP-B was investigated by the dialysis method[36]. Briefly, LNP-B was placed within a closed dialysis bag (Yuanye Bio-Technology, Shanghai, China) with a 100 kDa MWCO. The dialysis bag was sealed, immersed into 40 mL of PBS solution (pH 7.4, 0.01 mol/L) as the release medium in a 50 mL centrifuge tube, and incubated in a 37°C incubator with a constant oscillation. Sampling was conducted at specific time intervals, including 0.25, 0.5, 1, 2, 4, 8, 10, and 24 h. At each time point, 0.5 mL of PBS was withdrawn, and an equal volume of fresh PBS was added to maintain a constant system volume. The concentration of CDNs in the release medium was determined using HPLC, and the cumulative release of CDNs was calculated. For drug release in an acidic microenvironment, the procedure remained the same as described above, except that the release medium was switched from PBS to a sodium acetate buffer solution with a pH value of 5.0 or a Tris-HCl buffer solution with a pH value of 6.8[37].

2.5. *Cellular uptake of LNP-B by BMDCs*

Bone marrow-derived dendritic cells (BMDCs) were extracted from C57BL/6 mice as described previously[38]. BMDCs were plated in 12-well plates at the density of 2×10^6 cells per well and cultured with RPMI 1640 complete medium containing 10 ng/mL of IL-4 and 20 ng/mL of GM-CSF for 6 days.

For cellular uptake, BMDCs were seeded in 12-well plates at the density of 2×10^6 cells per well and cultured with RPMI1640 complete medium overnight. Then BMDCs were co-incubated with Cy5-CDN, Cy5-LNP-B, or Cy5-LNP-D (2.5 μmol/L of CDNs) for 0.5, 1, and 2 h, respectively. After washing with PBS, BMDCs were stained with FITC-CD11c antibody at 4°C for 15 min and subjected to flow cytometry (Beckman Counter, CA, USA). The mean fluorescence intensity (MFI) of CDNs in $CD11c^+$ cells was analyzed. For fluorescence imaging, BMDCs were stained with DAPI for 15 min and then imaged with a fluorescence microscope (Olympus CKX53 Inverted Phase Contrast Fluorescence Microscope, Olympus, Japan).

To observe the lysosomal escape of CDNs, BMDCs were seeded in confocal dishes at a concentration of 2×10^5 cells per dish overnight. Then, BMDCs were incubated with Cy5-LNP-B or Cy5-LNP-D for 0.5, 2, and 4 h, respectively. Following three washes with pre-cooled PBS, BMDCs were incubated with FITC-Lysotracker in the dark for 10 min, stained with DAPI for 15 min, and then subjected to fluorescence imaging with a fluorescence microscope (Olympus CKX53 Inverted Phase Contrast Fluorescence Microscope). The co-localization of CDNs and lysosomes was analyzed with Image J software (National Institutes of Health, USA).

2.6. *Activation of BMDCs by LNP-B*

For the assessment of the activation of BMDCs after LNP-B treatment, BMDCs cells were seeded in 12-well plates at the density of 2×10^6 cells per well and cultured overnight. Afterward, cells were incubated with CDNs, LNP-B, and LNP-D containing equal amounts of CDNs (2.5 μmol/L) for 8 h, respectively. For cytokine release tests, the cell culture medium was collected to determine the concentration of cytokines released by BMDCs including tumor necrosis factor-α (TNF-α), interferon-β (IFN-β), and interferon-γ (IFN-γ) using ELISA kits. For the measurement of DCs maturation, BMDCs after LNP-B treatment were washed three times with pre-cooled PBS, blocked with CD16/32 antibody for 15 min at room temperature, successively stained with fluorescence-labeled antibodies (FITC-anti-CD11c, PE-anti-CD80, and APC/Cyanine7-anti-CD86) for 15 min at 4°C and then subjected to flow cytometry (Beckman Counter). For Western blot analysis of typical proteins associated with the STING pathway, BMDCs after LNP-B treatment were washed with pre-cooled PBS, added with protease inhibitors and phosphatase inhibitors, and completely lysised by Triton X-100. Cellular proteins were extracted from the lysates using an ice-cold lysis buffer. Subsequently, 20 μg of total protein was loaded for SDS-polyacrylamide gel electrophoresis (PAGE) and then transferred to a polyvinylidene difluoride nitrocellulose membrane (Bio-Rad). After incubating with primary antibodies for p56-Nf-κB, p-p56-Nf-κB, TBK1, p-TBK1, IRF3, p-IRF3, and ACTIN, the membrane was probed with horseradish peroxidase (HRP)-conjugated secondary antibodies (R&D systems, USA), and detected using Immobilon™ Western Chemiluminescent HRP Substrate (Millipore, Bedford, MA, USA).

2.7. *Cellular uptake mechanism of LNP-B*

To investigate cellular uptake mechanism of LNP-B, CT26 cells as model cells were seeded in 12-well plates at a density of 2×10^6 per well, cultured overnight, and pretreated with various uptake inhibitors or inhibiting factors including 5 μg/mL of chlorpromazine (a coating depression inhibitor which inhibits clathrin assembly on endosomes and prevents assembly of coated caveolae on the cell surface), 100 μg/mL of genistein (an inhibitor of acupoint depression, reversibly inhibiting tyrosine kinase), 1.5 mg/mL of amiloride (a macropinocytosis inhibitor which inhibits Na^+/H^+ exchange and decreases intracellular pH), 6.5 mg/mL of β-cyclodextrin (a lipid raft inhibitor which removes cholesterol from membranes), 0.2 mg/mL of monensin (a lysosomal inhibitor which prevents the acidification and maturation of endosomes), 5 μg/mL of cytochalasin-D (a cytoskeleton-related inhibitor which binds to actin, inhibits polymerization, and induces actin depolymerization), and low temperature (4°C) for 2 h, respectively. Afterward, cells were incubated with Cy5-CDNs, Cy5-LNP-B, or Cy5-LNP-D for another 2 h, detached by trypsin digestion, collected by centrifugation, and subjected to flow cytometry (Beckman Counter).

2.8. *Repolarizing of BMDMs by LNP-B*

Bone marrow-derived macrophages (BMDMs) were generated using a similar method as BMDCs, with the exception that GM-CSF and IL-4 cytokines were replaced with M-CSF. BMDMs were pre-polarized to M2 phenotype (M2) by incubation with 20 ng/mL of mouse IL-4 and mouse M-CSF for 48 h, and untreated BMDMs were regarded as M0 macrophages. Afterward, BMDMs were seeded in 12-well plates at the density of 2×10^5 cells per well, cultured overnight, and incubated with CDNs, LNP-B, and LNP-D containing equal amounts of CDN (2.5 μmol/L) for 24 h. For flow cytometry analysis, BMDMs after LNP-B treatment were washed with pre-cooled PBS, blocked with FCAS solution, successively stained with fluorescence-labeled antibodies (FITC-anti-F4/80 antibody, PE-anti-CD86 antibody or Percp/Cy5-anti-CD206 antibody) as described above, and then subjected to flow cytometry (Beckman Counter). For testing cytokine release, the cell culture medium was collected to determine the concentration of cytokines secreted by M1 macrophages including TNF-α and IFN-β using ELISA kits.

2.9. *Tumor cell-inhibiting effect of activated BMDMs*

CT26 cells as model tumor cells were diluted to the optimized concentration of approximately 1.5×10^5 cells/mL and 10 μL of CT26 cells were added to the 96-well plate[39−41]. Afterward, 100 μL of LNP-B-treated BMDMs were added to the 96-well plate at an immune cell-to-tumor cell ratio of 20:1, resulting in a final volume of 110 μL. PBS-treated BMDMs were added to tumor cells as a control. Cells were cultured overnight in the complete DMEM medium, containing 10% FBS. A standard CCK8 assay was then performed in accordance with the manufacturer's instructions.

2.10. *Pharmacokinetics and biodistribution of LNP-B*

To observe the pharmacokinetics of different formulations, Cy5-CDNs, Cy5-LNP-B, and Cy5-LNP-D were injected into mice *via* the tail vein at the CDN dose of 10 μg. At different time points (1, 15, 30 min, 1, 4, 8, and 24 h) after injection, 50 μL of blood was taken from the orbit of mice and diluted with 50 μL of PBS. The fluorescence intensity (Ex/Em = 640/670 nm) of blood samples was detected by a microplate reader (TECAN M1000). The concentration-time curve was plotted and the half-live of CDNs was analyzed by DAS2.0 software (Shanghai, China).

To investigate the biodistribution of different formulations, Cy5-CDN, Cy5-LNP-B, and Cy5-LNP-D were intravenously injected into tumor-bearing mice at the CDN dose of 10 μg. At different time points after injection, mice were subjected to fluorescence imaging by the *in vivo* Imaging System (PerkinElmer). Twenty-four hours later, mice were sacrificed followed by heart perfusion with saline. Major organs, including the heart, liver, spleen, lung, kidneys, tumor, and TDLN were harvested and imaged with the *in vivo* Imaging System (PerkinElmer). Afterward, major organs were weighed, homogenized in PBS, and analyzed on a plate reader (TECAN M1000) to obtain the fluorescence intensity.

2.11. *Identification of immune cells taking up LNP-B*

To analyze LNP-B distribution in immune cells in the tumor, spleen, and TDLN. Cy5-CDNs, Cy5-LNP-B, and Cy5-LNP-D were injected intravenously into tumor-bearing mice at the CDN dose of 10 μg. At 6 h after injection, mice were sacrificed followed by heart perfusion with saline, and the spleen, tumor, and TDLN were collected for flow cytometry. In order to obtain splenocytes, the spleen was excised, manually disrupted, and filtered through a 70 μm cell strainer. The resulting cells were retrieved *via* centrifugation at 800×*g* for 3 min at 4°C and resuspended in 1 mL of red blood cell (RBC) lysis buffer prior to washing with PBS. Following labeling with cell-type specific markers ($CD45^+CD3^+$ T cells, $CD45^+CD19^+$ B cells, and $CD45^+CD11b^+CD11c^+MHCII^+$ DCs), the splenocytes were subjected to flow cytometry analysis. Isolation of tumor cells involved cutting the tumor into small fragments and incubating them in a sterile petri dish containing 3 mL of digest solution at 37°C for 60 min. After filtering through a 70 µm cell strainer to eliminate undigested and connective tissues, the resulting cell suspension was retrieved *via* centrifugation at 800×*g* for 5 min at 4°C and resuspended in 2 mL of FACS buffer. Cell suspensions from the tumor were then labeled with cell-type specific markers ($CD45^+CD3^-CD49b^+CD69^+$ NK cells, $CD45^+CD11b^+F4/80^+$ macrophages, $CD45^+CD11b^+CD11c^+MHCII^+$ DCs, and $CD45^+CD11b^+Ly6C^+$ MDSCs) and then subjected to flow cytometry analysis (Beckman Counter). Lymphocyte suspension was obtained and analyzed in the same way as the tumor tissue.

2.12. *Anti-tumor efficacy of LNP-B*

Tumor-bearing mice were randomly divided into four groups and received a single intravenous injection of indicated formulations (CDNs, LNP-B, LNP-D, and PBS) with the same CDN dose of 10 µg. The tumor size was measured every two days and the volume of the tumor was equal to the length times the width squared divided by two. The body weight of mice was also monitored every two days. On the 10th day, five mice from each group were sacrificed. The tumors were harvested, fixed with 4% paraformaldehyde, embedded in OCT compound, and cut into 10-µm slices. The slices were subjected to TdT-mediated dUTP Nick-End Labeling (TUNEL) staining and hematoxylin-eosin (H&E) staining according to routine protocols and imaged under a fluorescent microscope (Leica CM305, Germany).

2.13. *Anti-tumor immune responses*

Tumor-bearing mice were randomly divided into four groups, and respectively received a single intravenous injection of indicated formulations as described above. On the 3rd day, the tumor, spleen, and TDLN from each group were collected and placed on ice. Single-cell suspensions of tissues were prepared according to routine protocols, blocked with anti-CD16/32 antibody for 15 min, stained with cell type specific markers ($CD45^+CD11b^+CD11c^+$ $CD80^+CD86^+$ DCs, $CD45^+CD11b^+F4/80^+CD86^+$ M1 macrophages, $CD45^+CD11b^+F4/80^+CD206^+$ M2 macrophages, $CD45^+CD3^+CD8^+$ T cells, $CD45^+CD19^+IgD^+$ B cells, $CD45^+$ $CD11b^+Ly6C^+$ MDSCs, $CD45^+CD3^-CD49b^+CD69^+$ NK cells, and $CD45^+CD3^+CD4^+Foxp3^+CD25^+$ Tregs) according to the manufacturer's instructions, and analyzed by flow cytometry (Beckman Counter).

For the tumor cytokine test, the tumor tissue was extracted from the mice and weighed on the 3rd day. The tissue was subsequently mixed with pre-chilled PBS at a dilution ratio of 1 g−10 mL of PBS. Homogenization was performed using a freezer homogenizer, and the mixture was then centrifuged at 10,000×*g* at 4°C for 20 min. The supernatant was collected and filtered using a 5 µm needle filter to remove lipids. The resulting filtrate was used to determine the concentration of inflammatory factors (IFN-γ, IFN-β, and IL-6), following the instructions provided in the ELISA kit.

2.14. *Statistical analysis*

Data are expressed as mean ± standard deviation (SD). To test for differences among groups, one- or two-way ANOVA analysis was conducted. Statistical analyses were performed using GraphPad Prism 9.0 (GraphPad Software). $^*P < 0.05$; $^{**}P < 0.01$; $^{***}P < 0.001$; and ns means no difference between two groups.

3. Results and discussion

3.1. *Optimization of LNP-B*

The NMR hydrogen spectroscopy analysis indicated the successful synthesis of DSPE-PCB^+ (Supporting Information Figs. S1−S3). The verification of DSPE-PCB^+ degradation was achieved by monitoring the changes of the zeta potential of DSPE-PCB^+ under acidic conditions (Supporting Information Fig. S4). It was found that the positive surface potential of DSPE-PCB^+ micelles rapidly decreased from +50 mV to near neutrality after 2 h, indicating that DSPE-PCB^+ undergoes hydrolysis and transforms into the electrically neutral zwitterionic polymer. The results of the CCK8 experiment conducted on BMDCs and CT26 cells demonstrated that no cytotoxic effects were observed on DSPE-PCB^+ (Supporting Information Fig. S5). CDN-Mn@PCB nanoparticles were formed through self-assembly, primarily driven by the electrostatic interaction forces between positively charged DSPE-PCB^+, Mn^{2+}, and negatively charged CDNs. Thus, the percentage of cationic DSPE-PCB^+ could have a great impact on the structure of the nanoparticle and the loading capacity of CDNs. With the increasing percentage of DSPE-PCB^+, the diameter of CDN-Mn@PCB varied while the zeta potential did not show significant differences (Supporting Information Fig. S6A and S6B). When the N/P molar ratio was 4:1, CDN-Mn@PCB-2 showed smaller size (around 110 nm), higher encapsulated efficacy (about 78.2%), and higher loading capacity (about 7.11%) (Fig. S6B−S6D) than other CDN-Mn@PCB nanoparticles. Therefore, CDN-Mn@PCB-2 was utilized for the preparation of LNP-B. Since positively charged nanoparticles entering into the blood fluid would be cleared rapidly by the mononuclear phagocyte system and might disturb the cell membrane to cause some toxicities, a neutral lipid DOPC and a functional lipid DSPE-mPEG2k were used in LNP-B to shield the positive charges of CDN-Mn@PCB. Cholesterol is commonly incorporated into LNP to modify their physical properties. In order to achieve a stable and intelligent LNP, LNP-B with different amounts of cholesterol were prepared and characterized. It was found that the mean size of all LNP-B varied between 100 nm and 150 nm and the zeta potential varied from −20 and −30 mV (Fig. S6E and S6F). Importantly, cholesterol content greatly influenced the release behavior of CDNs from LNP-B. In the pH 7.4 environment, increasing the contents of cholesterol hindered the quick release of CDNs from the LNP-B. In the acid environment similar to lysosomes, decreasing the contents of cholesterol accelerated the release of CDNs from LNP-B (Fig. S6G and S6H). Since LNP-B with the molar ratio of DOPC to cholesterol of 1:1 (LNP-B2) was stable in the pH 7.4 environment but showed acid-sensitive release property in the pH 5.0 environment, it was selected for further study.

3.2. *Characterization of LNP-B*

For evaluating the impact of cationic lipids on the physiochemical properties of LNP, LNP-D made from DOTAP was prepared as a control with the same method as LNP-B which was the spherical form of the bilayer (Fig. 1A and Supporting Information Fig. S7). Compared with LNP-D, LNP-B had similar size, zeta potential, but higher loading capability (LC) (Fig. 1B−D) as a result of DSPE-PCB^+ retaining a higher positive charge density (17 cations per molar molecule) compared to DOTAP (1 cation per molar molecule). The encapsulation efficiency of manganese ions in

LNP-B was around 2.40%, with a loading capacity of 0.22%. Meanwhile, the encapsulation efficiency of manganese ions in LNP-D was approximately 3.00%, with a loading capacity of 0.21%. The size of LNP-B remained stable in PBS for a period of 9 days, while the size of LNP-D exhibited sharp fluctuations (Fig. 1E). Both LNP-B and LNP-D did not show any aggregation when incubated with 50% FBS for up to 12 h. However, after 24 h, LNP-B was still stable and LNP-D exhibited obvious instability (Fig. 1F). These results suggested that LNP-B may be more stable than LNP-D *in vivo*. CDNs need to be released from LNP-B to function, so we measured the release of drugs in different pH solutions. It was found that CDNs diffused quickly from dialysis bags in a pH 7.4 and pH 6.8 buffer, while LNP-B and LNP-D showed sustained release of CDNs (Fig. 1G and Supporting Information Fig. S8). The releasing rate of CDNs from LNP-B was much slower than LNP-D, suggesting that LNP-B probably has a more compact nanostructure and less leakage of CDNs during storage and circulation than LNP-D. In an acidic environment, LNP-B released CDNs at a slower rate compared to LNP-D. However, both LNP-B and LNP-D demonstrated faster CDNs release in pH 5.5 buffer compared to pH 7.4 and pH 6.8 buffer, indicating their acid-sensitive release properties (Fig. 1H). Overall, LNP-B exhibited superior stability and an acid-sensitive release property.

3.3. *Cellular uptake of LNP-B*

To activate the cGAS-STING pathway, CDNs must enter into the cells. As dendritic cells and macrophages were known to function as antigen presenting cells[42,43], bone marrow-derived dendritic cells (BMDCs) and bone marrow-derived macrophages (BMDMs) were selected to assess the cellular internalization of LNP-B. It was found that LNP-B and LNP-D significantly facilitated the uptake of CDNs by BMDCs and BMDMs, whereas a limited number of free CDNs were internalized by BMDCs and BMDMs due to their hydrophilic nature and impermeability to cell membranes (Fig. 2A–E). Interestingly, although LNP-B had a formulation similar to LNP-D except the cationic lipid, LNP-B showed significantly higher cellular uptake by BMDCs and BMDMs than LNP-D which may be due to the protein corona adsorbed on their surface. According to the analysis of the protein corona, it was shown that even though the phospholipid layer of LNP-B and LNP-D was the same, the composition of the protein corona on the nanoparticle surface demonstrated a difference. There were 39 proteins that showed significant differences between the two groups (Supporting Information Fig. S9A). Among them, compared with LNP-D, 31 proteins upregulated and 8 proteins downregulated in the protein corona of LNP-B (Fig. S9B). Combined with GO analysis, it was found that the elevated protein in the corona of LNP-B was mainly involved in the biological process of the immune system and played a binding function (Fig. S9C). This may facilitate LNP-B to be internalized by immune cells such as BMDCs and BMDMs[44].

In order to investigate the mechanism of cellular uptake, various inhibitors were employed. The uptake of Cy5-CDNs, Cy5-LNP-B, and Cy5-LNP-D was inhibited to varying degrees by different inhibitors, indicating that they enter the cell through multiple pathways, including clathrin-mediated endocytosis, caveolin-mediated endocytosis, and micropinocytosis. Notably, for free CDNs, low temperature, β-cyclodextrin, and genistein exhibited high inhibition rate (88.0%, 72.0%, and 60.0%, respectively), suggesting that cellular uptake of CDNs is dependent on energy and primarily mediated by caveolae proteins and lipid rafts. With regards to LNP-B, low temperature, monensin, genistein, and cytochalasin-D showed high cell inhibition rate (82.0%, 73.1%, 64.0%, and 72.2%, respectively), indicating that its cellular uptake is also energy-dependent and heavily reliant on caveolin-mediated endocytosis, micropinocytosis, lipid rafts, and lysosomal transport. As for LNP-D, low temperature, β-cyclodextrin, amiloride, monensin, genistein, and cytochalasin-D

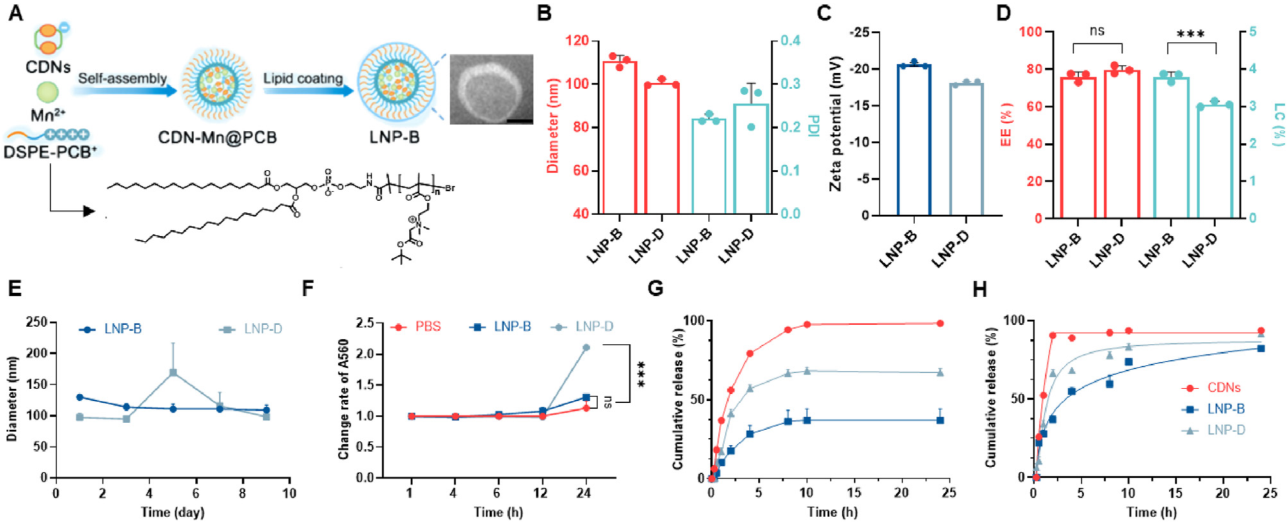

Figure 1 Characterization of LNP-B ($n = 3$). (A) Structure of DSPE-PCB$^+$ and schematics of preparation process and TEM of LNP-B, scale bar = 50 nm. (B) Mean diameter and polydispersity (PDI), (C) mean zeta potential, (D) encapsulation efficiency (EE), and loading capability (LC) of LNP-B and LNP-D. (E) Stability of LNP-B and LNP-D in pH 7.4 PBS over a span of 9 days. (F) Stability of LNP-B and LNP-D in 50% FBS over a span of 24 h. Drug release of LNP-B and LNP-D in (G) pH 7.4 PBS and (H) pH 5.0 buffer. Data are expressed as mean ± SD. One-way ANOVA analysis was conducted to test for differences among groups. ***$P < 0.001$; ns, no difference between two groups.

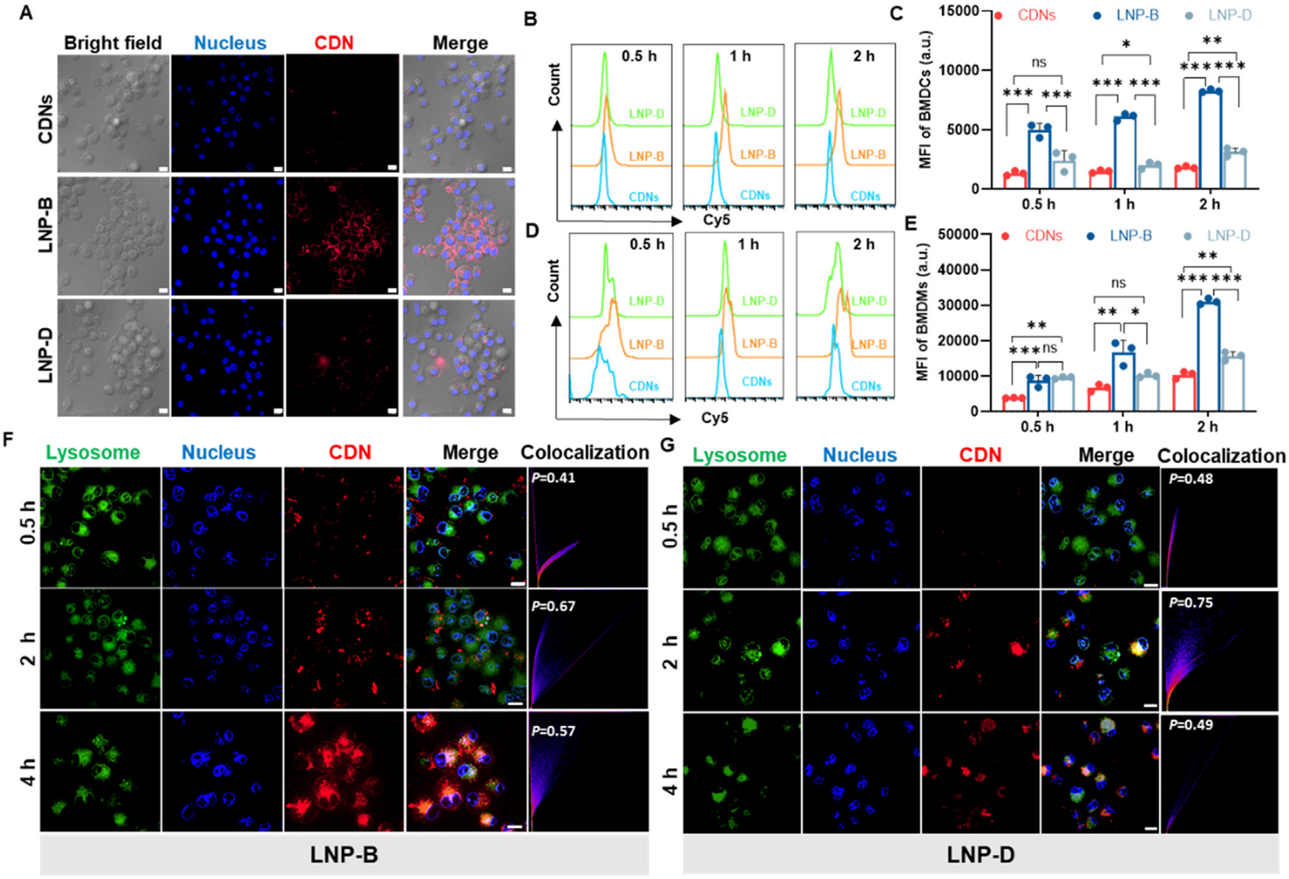

Figure 2 Cellular uptake of LNP-B *in vitro*. (A) Representative fluorescence images of BMDCs after incubation with LNP-B for 2 h. (B) Representative flow chart and (C) mean fluorescence intensity (MFI) of BMDCs after incubation with LNP-B for different times ($n = 3$). (D) Representative flow chart and (E) MFI of BMDMs after incubation with LNP-B for different times ($n = 3$). (F) Representative co-localization images and analysis of lysosomes and CDNs in BMDCs after incubation with LNP-B for different times. (G) Representative co-localization images and analysis of lysosomes and CDNs in BMDCs after incubation with LNP-D for different times and the corresponding fluorescence intensity profiles of CDNs and lysosomes along the dotted white line. Scale bar = 10 μm ($n = 3$). Data are expressed as means ± standard deviation (SD). One-way ANOVA analysis was conducted to test for differences among groups. $^*P < 0.05$, $^{**}P < 0.01$, and $^{***}P < 0.001$. ns, no significant difference between two groups.

exhibited high inhibition rate (82.1%, 71.0%, 66.0%, 65.0%, 71.1%, and 60.0%, respectively), highlighting that its entry into cells is largely dependent on energy and mainly relies on caveolin-mediated endocytosis, micropinocytosis, lipid rafts, and lysosomal transport (Supporting Information Fig. S10 and Table S1).

Encapsulation by LNP not only could change the cellular entry of CDNs, but also could alter the intercellular transport of CDNs. Once inside cells, LNPs would accumulate within lysosomes, whereas CDNs require binding to STING on the endoplasmic reticulum. As a result, it is anticipated that LNPs have the potential to evade acidic lysosomes responsible for receiving cargoes from the plasma membrane for degradation or recycling[45]. The positively charged lipids in LNP-B and LNP-D were used to interact with the negatively charged lysosomal membranes in acidic lysosomes, thereby reducing the stability of the lysosomal membranes and facilitating CDNs escape from the lysosome. After a co-incubation period of 0.5 h, it was observed that LNP-B was predominantly located on the cellular membrane. With the increase in incubation time to 2 h, LNP-B was found to be primarily located within the lysosomes. It was noted that the Pearson correlation coefficient reached its peak value of 0.67, indicating a strong association between LNP-B and the lysosomal compartment. After 4 h, LNP-B was observed to have spread throughout the entire cell, having successfully evaded lysosomal compartments (Fig. 2F). LNP-D, although less taken up by cells, exhibited similar behavior (Fig. 2G). It has been demonstrated that cholesterol can promote membrane fusion of nanoparticles[46] and stabilize the inverted hexagonal phase[47]. Therefore, it is hypothesized that when LNP-B enters into lysosomes, fusion of nanoparticles and lysosomal membranes begins[48]. Additionally, in acidic conditions of lysosomes, the ester bond of DSPE-PCB$^+$ consumes hydrogen ions for degradation to form DSPE-PCB, which can further consume hydrogen ions[49]. It is possible that membrane fusion and proton pump effects make LNP-B capable of lysosomal escape. Therefore, LNP-B could enhance cellular uptake of CDNs and facilitate CDNs escape from the lysosome.

3.4. *Activation of BMDCs by LNP-B*

CDNs released from LNP in the cytoplasm could activate the STING pathway which could induce the maturation of BMDCs[50]. CD80 and CD86 were the maturation markers of BMDCs[51]. It has been shown that manganese ion alone can stimulate the STING pathway. In order to investigate whether Mn^{2+} in the LNP could activate the STING pathway, the effect of Mn^{2+} with an equal dose to Mn^{2+} in LNP-B (2.0 μmol/L) on the maturation of BMDCs was assessed. As shown in Supporting Information Fig. S11, Mn^{2+} alone could not significantly increase the maturation of BMDCs, which may be due the Mn^{2+} concentration is not sufficient to activate the STING pathway[30,31]. The addition of Mn^{2+} to CDNs could not significantly increase maturation of BMDCs compared with CDNs alone. Considering that this dose of Mn^{2+} could not activate the STING pathway, we did not include the Mn^{2+} group in the subsequent experiments. Then we investigated whether LNP-B could activate STING pathways on BMDCs. The results demonstrated that LNP-B or LNP-D induced a much higher percentage of maturation in BMDCs compared to CDNs (Fig. 3A—D). This could be attributed to a higher cellular uptake of LNP-B or LNP-D compared to CDNs. There was no difference in BMDCs activation between LNP-B and LNP-D,

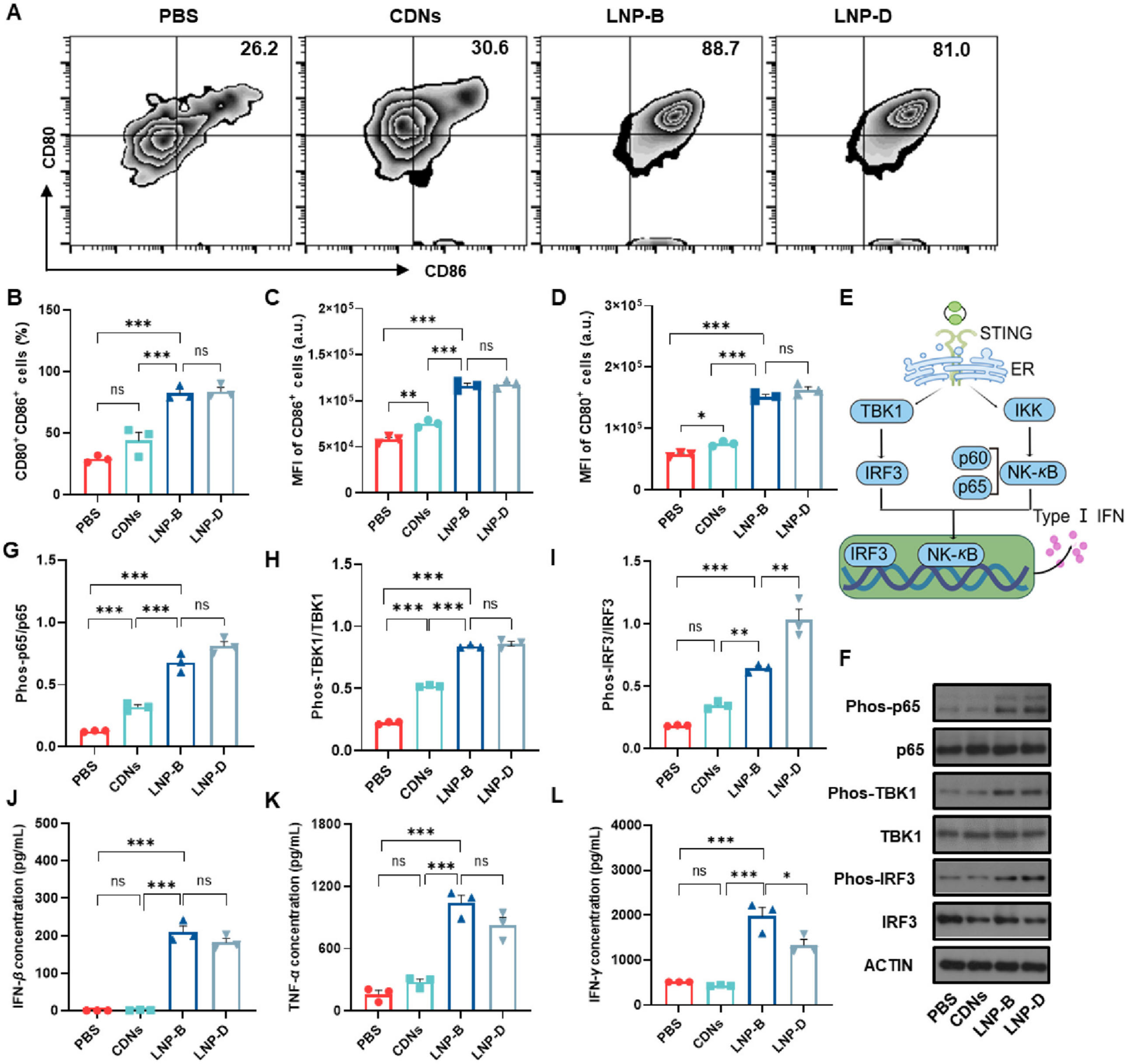

Figure 3 Activation of BMDCs *in vitro*. (A) Representative flow chart of $CD80^+$ and $CD86^+$ cells in BMDCs after incubation with LNP-B for 8 h, (B) Percentages of $CD80^+CD86^+$ cells, mean fluorescence intensity (MFI) of (C) $CD86^+$ cells and (D) $CD80^+$ cells in BMDCs after incubation with LNP-B for 8 h ($n = 3$). (E) Schematic diagram of LNP-B to activate STING pathway (created with Figdraw). (F) Western blot analysis of the expressions of key proteins of the STING pathway in BMDCs including p65, phos-p65, TBK1, phos-TBK1, IRF3, and phos-IRF3 after incubation with LNP-B. β-Actin was used as the loading control. Relative protein expression of Western blot analysis in BMDCs (G) phos-p65/p65 (H) phos-TBK1/TBK1 (I) phos-IRF3/IRF3 ($n = 3$). (J) IFN-β, (K) TNF-α, and (L) IFN-γ levels in the cell culture medium after BMDCs were treated with LNP-B ($n = 3$). Data are expressed as means ± SD. One-way ANOVA analysis was conducted to test for differences among groups. $^*P < 0.05$; $^{**}P < 0.01$; $^{***}P < 0.001$; and ns, no difference between two groups.

possibly due to uptake saturation of the LNP by BMDCs at 8 h[52,53]. The Western blot results revealed that the expression levels of phos-TBK1, phos-p65, and phos-IRF3 in LNP-B- or LNP-D-treated BMDCs were significantly higher compared to CDNs- or PBS-treated BMDCs (Fig. 3E–I). These results suggest that the STING pathway in BMDCs is activated upon treatment with LNP-B or LNP-D. Activation of the STING pathway can lead to the release of type I interferon (such as IFN-β) and induce the release of other anti-tumor cytokines, such as TNF-α and IFN-γ[54,55]. IFN-β plays a crucial role as a type I interferon in upregulating major tissue compatibility complex class I (MHC I) proteins and boosting the expression of tumor-associated antigens (TAA). This, in turn, leads to increased recognition and uptake of TAA by antigen-presenting cells and facilitates antigen presentation to cytotoxic T cells ($CD8^+$ T)[56]. TNF-α, on the other hand, acts as an inflammatory factor that triggers the necrosis of tumor cells and has the potential to impede tumor growth[57]. IFN-γ is known for its ability to inhibit the growth of tumors, promote cell death, and stimulate the immune system to combat tumor development[58]. It was shown that LNP-B or LNP-D treatment significantly upgraded the release of IFN-β, TNF-α, and IFN-γ in BMDCs compared with CDNs or PBS (Fig. 3J–L). Collectively, these findings indicate that LNP-B or LNP-D enhances BMDCs maturation and induces a robust activation of the STING pathway in BMDCs.

3.5. *Repolarizing of pro-tumor macrophages by LNP-B in vitro*

Not all macrophages in tumors were anti-tumor fighters. Some macrophages, when exposed to tumor-related stimuli, would switch their functional orientation and promote tumor growth and invasion. In a STING-dependent manner, STING agonists repolarize M2 pro-tumor macrophages into M1 anti-tumor macrophages[59]. To test whether LNP-B could repolarize the M2-BMDMs ($F4/80^+CD206^+$) to M1-BMDMs ($F4/80^+CD86^+$), M0-BMDMs were induced to M2-BMDM. Interestingly, CDNs, LNP-B, and LNP-D could repolarize M2-BMDMs, but LNP-B and LNP-D increased the percentage of M1-BMDMs more than free CDNs (Fig. 4A–E). ELISA results demonstrated that LNP-B or LNP-D treatment induced greater release of TNF-α and IFN-β from BMDMs compared to CDNs treatment (Fig. 4F and G). *In vitro* cytotoxicity testing further demonstrated that BMDMs

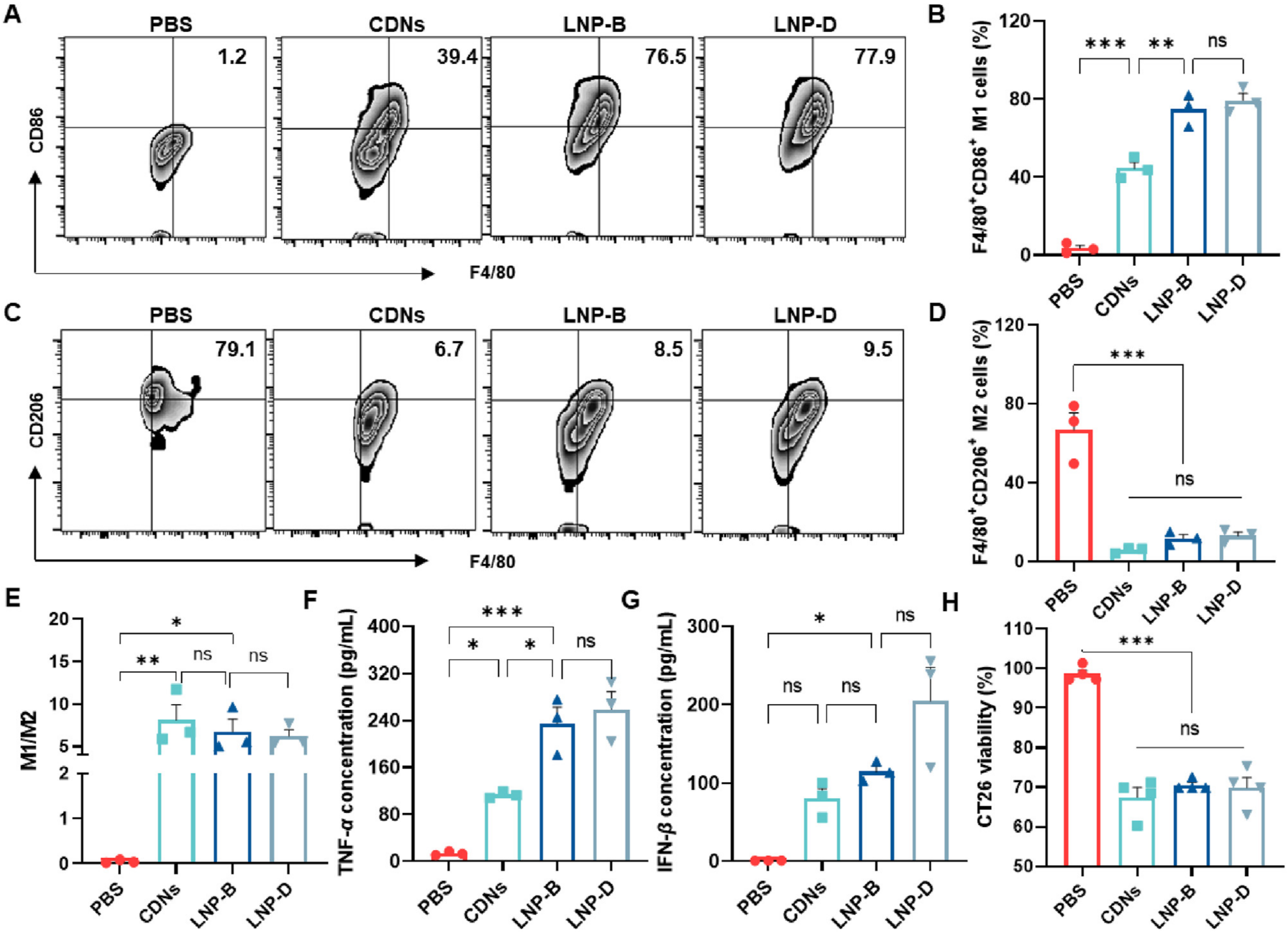

Figure 4 Repolarizing of pro-tumor macrophages *in vitro*. (A) Representative flow chart of $F4/80^+CD86^+$ cells and (B) quantification of the percentage of M1-like BMDMs in BMDMs after different treatments ($n = 3$). (C) Representative flow chart of $F4/80^+CD206^+$ cells and (D) quantification of the percentage of M2 BMDMs in BMDMs after different treatments. (E) Quantification of the ratio of M1/M2 macrophages in BMDMs after different treatments ($n = 3$). (F) TNF-α and (G) IFN-β levels in the cell culture medium after BMDMs were treated with different formulations ($n = 3$). (H) Cytotoxicity assay of LNP-B-treated BMDMs on CT26 cells ($n = 4$). Data are expressed as mean ± SD. One-way ANOVA analysis was conducted to test for differences among groups. $^*P < 0.05$; $^{**}P < 0.01$; $^{***}P < 0.001$; and ns, no difference between two groups.

treated by LNP-B or LNP-D could inhibit the growth of CT26 cells (Fig. 4H). Overall, these findings indicate that LNP-B or LNP-D repolarizes M2-macrophages to M1-macrophages.

3.6. *Pharmacokinetics and biodistribution of LNP-B*

LNP-B and LNP-D represented splendid performance in increasing the function of CDNs *in vitro*. To observe the behavior of LNP-B *in vivo*, Cy5-CDNs were used to prepare LNP-B and LNP-D. As shown in Fig. 5A and B, and Supporting Information Table S2, the encapsulation of CDNs within LNP tremendously improved their pharmacokinetics. Encapsulation in LNP-B increased the half-life of CDNs from its original duration of approximately 3.9 min to about 21.2 h, resulting in a 309-fold increase. After intravenous injection in healthy mice, LNP-B or LNP-D were found to be predominantly deposited in the liver and spleen, whereas the free CDNs primarily accumulated in the kidney (Supporting Information Fig. S12A−S12D). Upon intravenous injection in mice with tumors, LNP-B or LNP-D exhibited a progressive accumulation in the tumor over time, whereas minimal CDNs distributed to the tumor (Fig. 5C and D). The *ex vivo* fluorescence imaging demonstrated that both LNP-B and LNP-D displayed predominant accumulation in the liver, spleen, and tumor, whereas free CDNs exhibited minimal distribution to the tumor after intravenous injection (Fig. 5E). More importantly, both LNP-B and LNP-D displayed higher accumulation in TDLN compared to free CDNs (Fig. 5F and G). Further quantification of biodistribution agreed well with the *ex vivo* fluorescence imaging results (Fig. 5H). Based on the protein mass spectrometry results (Supporting Information Table S3), the proteins of the protein corona on LNP-B and LNP-D were mainly dysopsonins, such as albumin and apolipoproteins (Apo), which can inhibit phagocytosis and extend the circulation duration of nanoparticles[60], endowing them with long circulation ability which can help them target to extrahepatic tissues. In detail, Apo E, which could interact with the LDL receptor (LDL-R) and LDL-R-related protein abundantly present on liver hepatocytes[61,62], is positioned at the 9th and 15th place in the protein corona of LNP-D and LNP-B, respectively. Additionally, transferrin and vitronectin were found to adsorb on the surface of LNP-B and LNP-D.

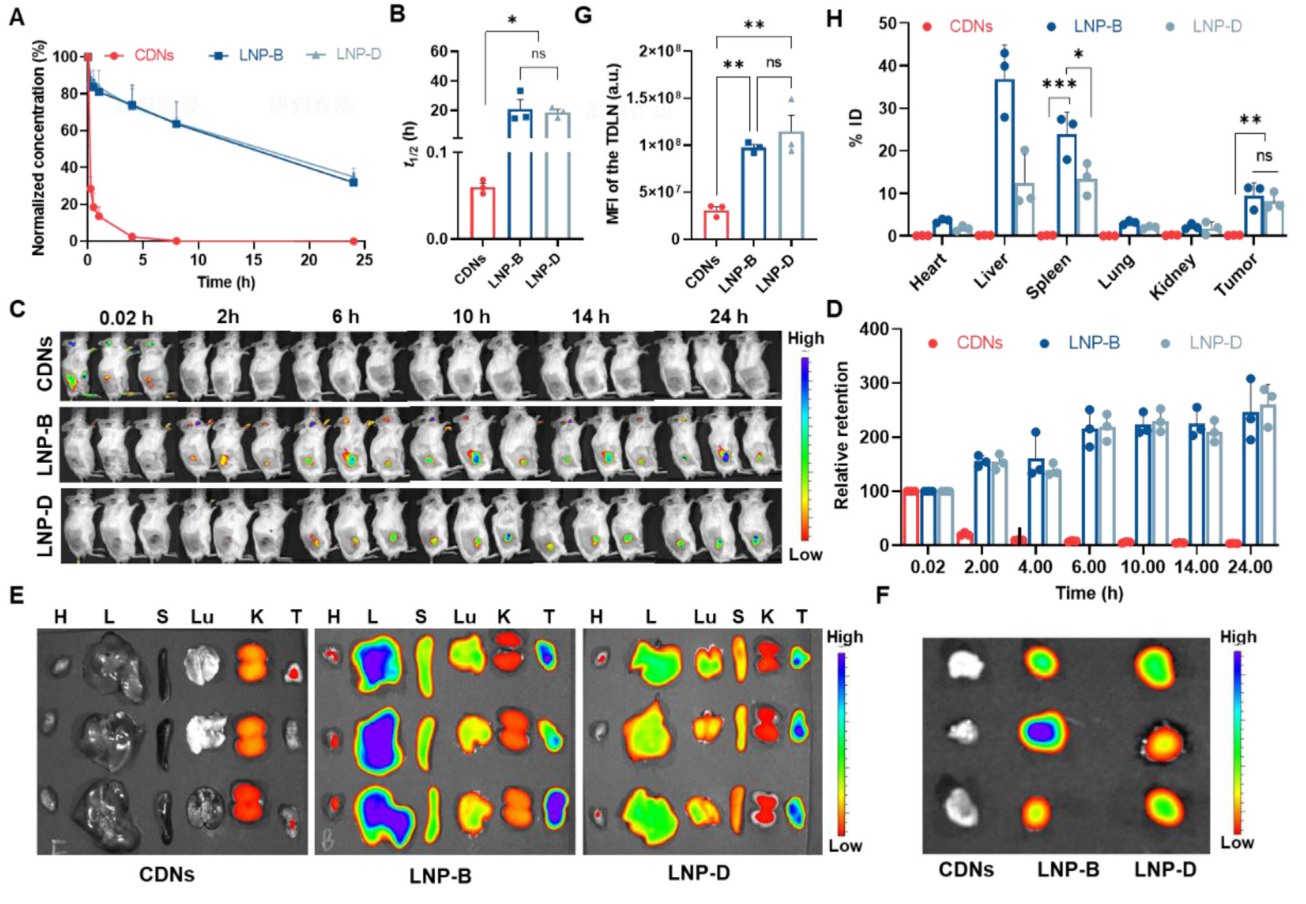

Figure 5 Pharmacokinetics and biodistribution of LNP-B. (A) CDN concentrations in the plasma as a function of time and (B) the elimination half-life of CDNs after intravenous injection of different formulations ($n = 3$). (C) Representative fluorescence images of tumor-bearing mice and (D) the corresponding fluorescence intensity of the tumors at different time points after intravenous injection of different formulations ($n = 3$). (E) *Ex vivo* fluorescence images of major organs at 24 h after intravenous injection of different formulations. H, L, S, Lu, K, and T referred to the heart, liver, spleen, lung, kidneys, and tumor, respectively. (F) *Ex vivo* fluorescence images of tumor draining lymph nodes (TDLN) and (G) the corresponding mean fluorescence intensity (MFI) of TDLN at 24 h after intravenous injection of different formulations ($n = 3$). (H) Quantification of biodistribution at 24 h after intravenous injection of different formulations ($n = 3$); Data are presented as % ID (percentage of injected dose). Data are expressed as mean ± SD. One-way ANOVA analysis was conducted to test for differences among groups. $^{*}P < 0.05$; $^{**}P < 0.01$; $^{***}P < 0.001$; and ns, no difference between two groups.

These proteins could bind to transferrin receptors[63,64] and integrins[65,66] respectively, which are highly expressed on tumor cells[67,68] and tumor vasculatures[69] respectively. These characteristics render LNP-B or LNP-D an effective targeting agent for tumors. The negative potential on the surface of LNP-B and LNP-D and the particle size of around 100 nm make them easy to target the spleen[70]. In general, it was the physical and chemical properties of LNP that endowed them targeting ability to the liver, spleen, and tumor[71]. Given the immunosuppressive nature of the tumor environment, a substantial accumulation of CDNs within the tumor could yield significant benefits in terms of anti-tumor effects. Moreover, the CDNs that accumulated in the spleen could trigger systemic immune responses within the body. Situated downstream of the tumor, TDLN harbors a diverse array of immune cells such as DCs, T cells, and B cells. This distinctive positioning of the TDLN, coupled with the presence of these immune cells, designates it as a pivotal site for mounting the systemic anti-tumor immune response. Undoubtedly, LNP-B or LNP-D improved the half live of CDNs and promoted the entry of CDNs into the tumor, spleen, and TDLN to activate the STING pathway in immune cells, which would prove beneficial in bolstering the anti-tumor immune response.

3.7. *Identification of immune cells taking up LNP-B within the tumor, spleen, and TDLN*

A number of cell types were present in the tumors, including macrophages, lymphocytes, natural killer cells (NK) and DCs which were responsible for generating an anti-tumor immune response. However, their activity was suppressed by immunosuppressive cells, including MDSCs which are inherently linked to the development of the TIME[72]. It was hypothesized that the intravenous administration of LNP-B would prompt immune cells within tumors to internalize CDNs, thereby leading to a reduction in the presence of immunosuppressive cells and a concurrent increase in the population of anti-tumor immune

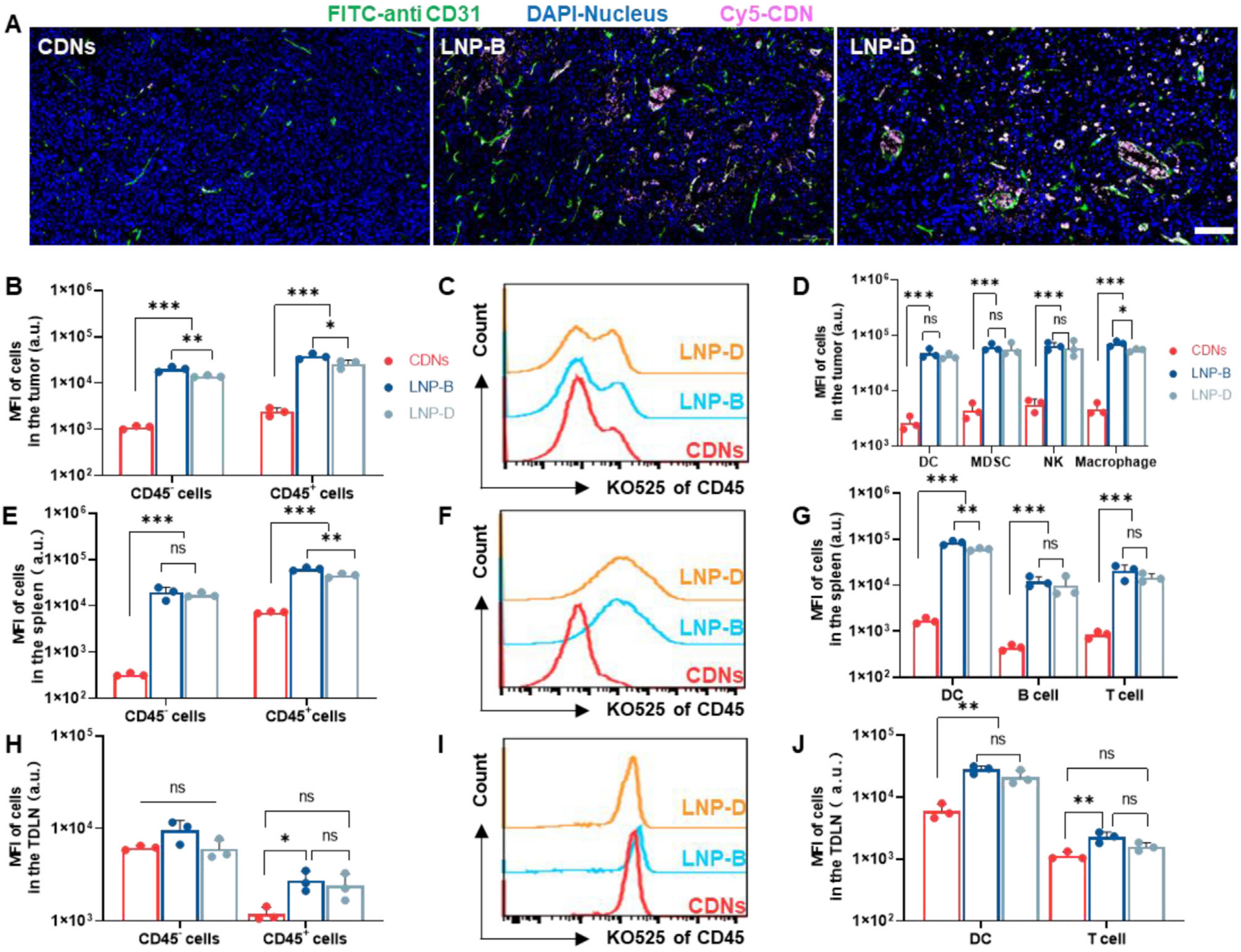

Figure 6 Identification of immune cells taking up LNP-B within the tumor, spleen, and TDLN. (A) Representative fluorescence images of tumor slices at 6 h after intravenous injection of Cy5-CDNs, Cy5-LNP-B, and Cy5-LNP-D. Scale bar = 100 μm. (B) Mean fluorescence intensity (MFI) of cells, (C) representative flow chart of $CD45^+$ cells, and (D) MFI of DCs, MDSCs, NK cells, and macrophages in the tumor at 6 h after intravenous injection of different formulations ($n = 3$). (E) MFI of cells, (F) representative flow chart of $CD45^+$ cells, and (G) MFI of DCs, B cells, and T cells in the spleen at 6 h after intravenous injection of different formulations ($n = 3$). (H) MFI of cells, (I) representative flow chart of $CD45^+$ cells, and (J) MFI of DCs and T cells in the TDLN at 6 h after intravenous injection of different formulations ($n = 3$). Data are expressed as mean ± SD. One-way ANOVA analysis was conducted to test for differences among groups. $^*P < 0.05$; $^{**}P < 0.01$; $^{***}P < 0.001$; and ns, no difference between two groups.

cells. To explore the internalization of LNP-B within tumors, investigations were carried out to determine which immune cells were involved in the uptake of LNP-B. Fluorescence imaging of tumor slices demonstrated that LNP-B or LNP-D were predominantly distributed within both tumor blood vessels and the tumor parenchyma (Fig. 6A). Interestingly, regardless of the administration of CDNs, LNP-B, or LNP-D, they were predominantly internalized by CD45$^+$ cells in the tumor. Additionally, the endocytosis of LNP-B and LNP-D by CD45$^+$ cells far exceeded that of CDNs (Fig. 6B and C). CD45$^+$ cells were then classified into DCs, MDSCs, NK cells, and macrophages. Overall, these cells showed significantly higher uptake of LNP-B or LNP-D compared to CDNs (Fig. 6D). As the largest peripheral immune organ, the spleen plays a crucial role in the systemic immune response. The white blood cells in the spleen include various T cells, B cells, and DCs. B cells and DCs, which absorb and transmit antigens and migrate to the white pulp of the spleen to promote antigen presentation to lymphocytes, activating humoral immune responses and cellular immune responses[73]. TDLN is the main site of anti-tumor immune development, and activated intratumor DCs reach TDLN through lymphatic vessels. Because DCs present TAA to activate T cells, an adaptive anti-tumor immune response is produced[74]. Hence, we investigated the specific immune cell population responsible for the uptake of LNP-B in the spleen. Following intravenous injection, both LNP-B and LNP-D were predominantly taken up by CD45$^+$ cells in the spleen (Fig. 6E and F). Notably, they exhibited far higher levels of cellular uptake in all cell types, including DCs, T cells, and B cells, compared to CDNs (Fig. 6G). Additionally, we observed the cellular uptake of LNP-B by immune cells in the TDLN. Both LNP-B and LNP-D were predominantly internalized by CD45$^-$ cells in the TDLN (Fig. 6H and I). Interestingly, both LNP-B and LNP-D exhibited higher levels of cellular uptake in DCs and T cells compared to CDNs (Fig. 6J). Furthermore, the uptake of LNP-B and LNP-D by DCs was considerably greater compared to their uptake by T cells. In general, the above results indicate that LNP-B exhibits excellent targeting towards immune cells in the tumor, spleen, and TDLN, as it is efficiently taken up by these immune cells. This uptake is expected to enhance the activation of the STING pathway within immune cells, thereby promoting both humoral and cellular immune responses and exerting anti-tumor effects.

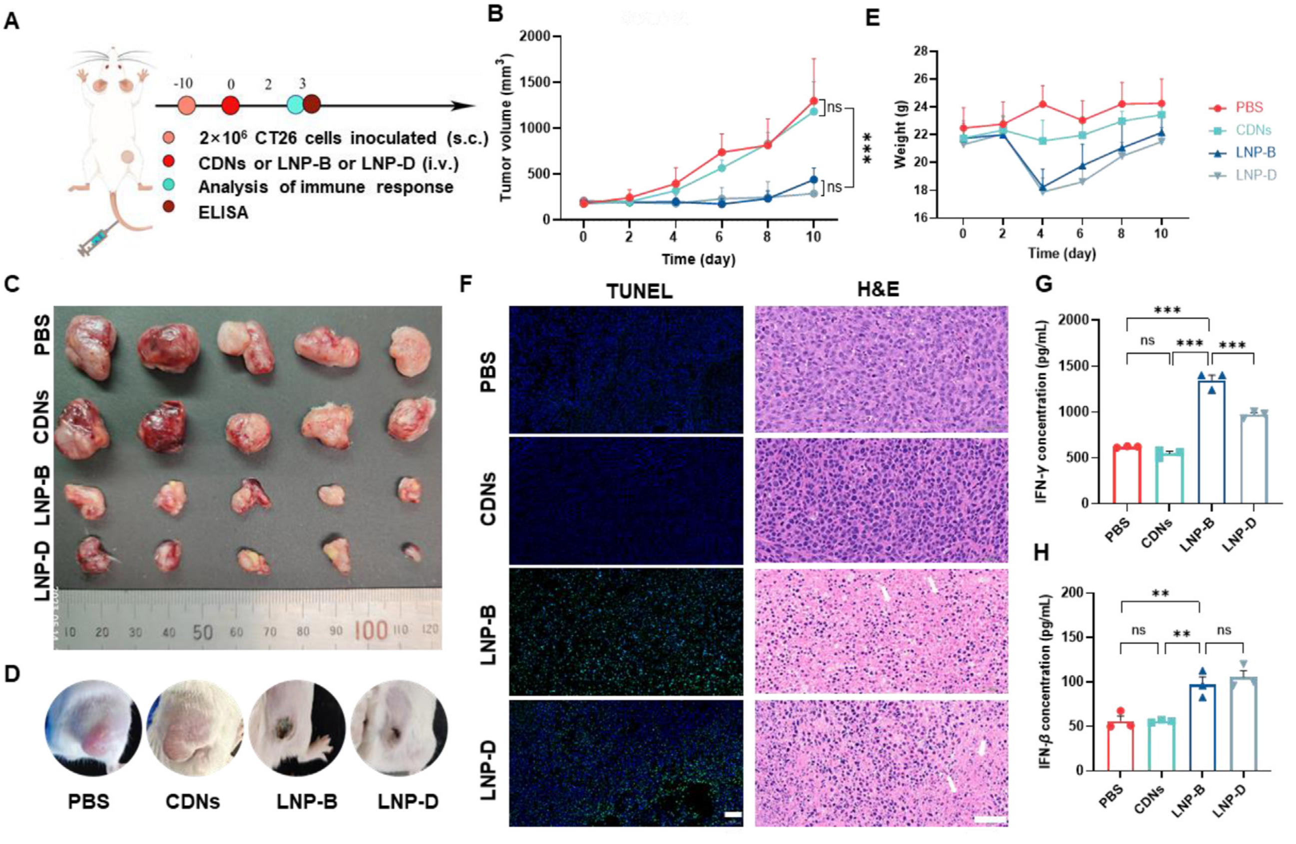

Figure 7 Anti-tumor efficacy of LNP-B. (A) Schematic diagram of the treatment cycle and test items (created with Figdraw). (B) The tumor volume was plotted with time after different treatments ($n = 5$). When the tumor volume was above 1500 mm^3, the study was ended. (C) Photos of *ex vivo* tumors at the end of this study. (D) Typical images of tumor models on the 10th day. (E) The body weight changes after different treatments ($n = 5$). (F) Representative images of tumor slices after TUNEL staining (left panel, Scale bar = 100 μm) and H&E staining (right panel, Scale bar = 50 μm) on the 3rd day after different treatments. Green signals indicated cell apoptosis, and blue signals indicated cell nuclei. The white arrow refers to the contraction and loss of the tumor nucleus. (G, H) Expression levels of (G) IFN-γ and (H) IFN-β in tumors quantified by ELISA on the 3rd day after different treatments ($n = 3$). Data are expressed as mean ± SD. One-way ANOVA analysis was conducted to test for differences among groups. *$P < 0.05$; **$P < 0.01$; ***$P < 0.001$; and ns, no difference between two groups.

3.8. *Anti-tumor efficacy of LNP-B*

Firstly, the safe dosage range of intravenous CDNs was investigated in normal BALB/c mice. As shown in Supporting Information Fig. S13, in normal mice, the lethal dose of ADU-S100 was 31.6 μg. At a dose of 20 μg, the mice developed symptoms of hair disorder and poor condition in the first 24 h, and gradually recovered in the later stages, indicating that the maximum tolerated dose of intravenous CDNs is around 20 μg. Therefore, a dose of 20 μg of CDNs was chosen as the therapeutic dose in CT26 tumor-bearing mice. As shown in Supporting Information Fig. S14, free CDNs exhibited a tumor suppression rate of 37.9% at a dose of 20 μg, while LNP-B exhibited an inhibition rate of 80.9%. Although LNP-D exhibited an inhibition rate of 98.2%, the mice showed a drastic drop in body weight and two out of five tumor-bearing mice (40%) died on Day 4. We also observed that the feces of the surviving mice in the LNP-D group were unformed and black in color, and did not gradually recover until the 8th day after dosing. Similar results were also found in Wehba's work[26]. Therefore, these results indicate that the maximum tolerated dose of LNP-D is less than 20 μg while that of LNP-B is greater than 20 μg, and the therapeutic window for free CDNs is from more than 20 μg to less than 31.6 μg. To facilitate a more accurate comparison of tumor inhibition among various treatment groups while ensuring safety, a dosage of 10 μg of CDNs was chosen for subsequent efficacy evaluations (Fig. 7A).

Compared with CDNs and PBS, LNP-B and LNP-D (10 μg of CDNs) significantly inhibited CT26 tumor growth (Fig. 7B−D and Supporting Information Fig. S15), with tumor inhibition rates reaching 73.0% and 83.7% ($P > 0.05$), respectively. Although the body weight of LNP-B- and LNP-D-treated mice decreased after injection, but it gradually recovered with time (Fig. 7E). To further confirm the efficacy of LNP-B in inhibiting tumor growth, tumor samples were obtained and subjected to histological analysis using H&E staining. The tumor tissue sections of the LNP-B and LNP-D groups exhibited extensive nuclear damage and loss (Fig. 7F). Additionally, TUNEL staining of tumor sections revealed that the signals of cell apoptosis in the LNP-B and LNP-D groups were much stronger than those in the CDNs and PBS groups, indicating a higher level of apoptosis after LNP-B and LNP-D treatments. In addition, it was observed that LNP-B and LNP-D significantly amplified the expression levels of anti-tumor cytokines including IFN-γ, IFN-β, and IL-6, within the tumor microenvironment, in contrast to CDNs and PBS (Fig. 7G−H and Supporting Information Fig. S16). Importantly, both IFN-β and IFN-γ play crucial roles in attracting CD8$^+$ T cells through the chemokine

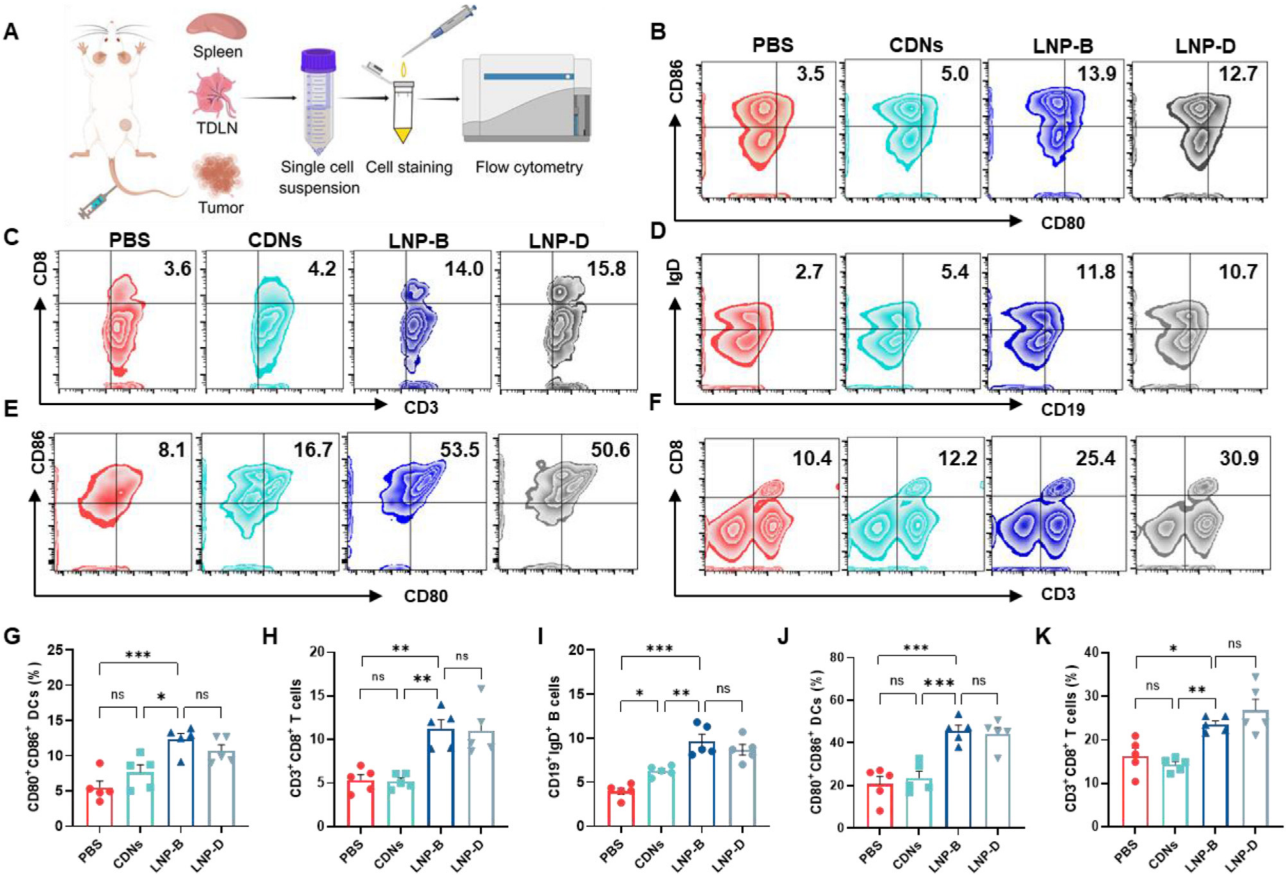

Figure 8 Immunoassay of the spleen and the TDLN after LNP-B treatment ($n = 5$). (A) Schematic diagram of the immunoassay process by Figdraw. (B−D) Representative flow cytometry plots of splenic immune cells including (B) CD$^+$80CD86$^+$ DCs, (C) CD3$^+$CD8$^+$ T cells, and (D) CD19$^+$IgD$^+$ B cells after different treatments, and (G−I) the quantitative analysis of these splenic immune cells after different treatments. (E, F) Representative flow cytometry plots of immune cells including (E) CD80$^+$CD86$^+$ DCs and (F) CD3$^+$CD8$^+$ T cells in TDLN and (J, K) the quantitative analysis of these immune cells in TDLN after different treatments. Data are expressed as mean ± SD. One-way ANOVA analysis was conducted to test for differences among groups. $^*P < 0.05$; $^{**}P < 0.01$; $^{***}P < 0.001$; and ns, no difference between two groups.

CXCL10, as well as enhancing the cytotoxicity of NK cells. Simultaneously, they inhibit the function of immune cells that promote tumor growth, such as MDSCs and Tregs[75,76]. To investigate if the anti-tumor effect persists upon reducing the LNP dosage, we employed a CDNs dose of 5 μg for the investigation. As shown in Supporting Information Fig. S17, at a CDNs dose of 5 μg, LNP-B and LNP-D showed a similar tumor suppression rate (68.8% *vs* 66.2%, $P > 0.05$) without significant weight changes. These results indicate that the therapeutic window of LNP-B spans from less than 5 μg to over 20 μg. In summary, LNP-B undoubtedly broadens the therapeutic window of CDNs, is better tolerated than LNP-D, and has superior anti-tumor efficacy.

3.9. *Anti-tumor immune responses of LNP-B*

Based on the above results that LNP-B could potentiate the anti-tumor effect of CDNs in CT26 tumor-bearing mice, we further explored the mechanisms underlying the therapeutic effects of LNP-B by examining the immune microenvironment of the spleen, TDLN, and tumor. Three days following intravenous injection of PBS, CDNs, LNP-B, and LNP-D, the spleen, TDLN, and tumor were harvested for immune cell analysis (Figs. 8 and 9). Analyzed by flow cytometry (Fig. 8A), it was shown that a much higher percentage of mature DCs were observed in the spleen of LNP-B-treated mice, compared with PBS, free CDNs or LNP-D-treated mice (Fig. 8B and G). Subsequently, we assessed the extent of T cell activation. Consistent with our expectations, the most pronounced level of $CD8^+$ T cell activation was observed in the LNP-B group (Fig. 8C and H). Then splenic follicular B cells were investigated, which possessed the capacity to exude a substantial proportion of high-affinity antibodies and engaged in interactions with T follicular helper cells[77]. It was found that LNP-B and LNP-D led to a significant increase in the B cell population compared to PBS and CDNs (Fig. 8D and I). Next, we studied the immune responses in the TDLN. Similarly, LNP-B and LNP-D led to a higher percentage of DC maturation compared to PBS and CDNs (Fig. 8E and J). Consistent with expectations, enhanced activation levels were observed in $CD8^+$ T cells within the TDLN of mice treated with LNP-B or LNP-D, in comparison to mice treated with PBS or CDNs (Fig. 8F and K). Based on the aforementioned findings, both LNP-B and LNP-D exhibited a higher capability in activating systemic immunity compared to CDNs and PBS, which is beneficial for anti-tumor immunotherapy.

Tumor immunotherapy has had a significant impact in clinical settings. However, it has been observed that only a group of patients shows positive responses to immunotherapy due to their

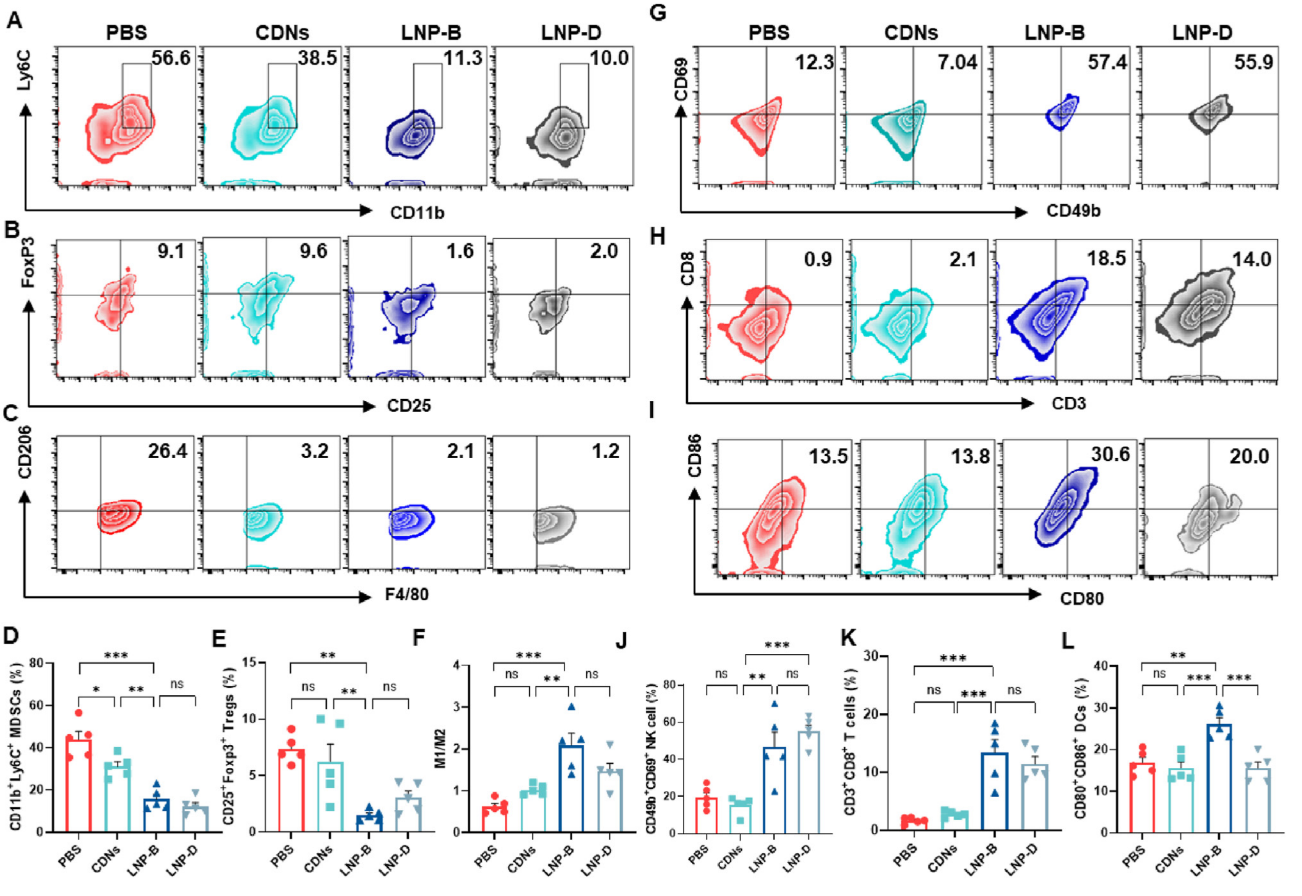

Figure 9 Immunoassay of the tumor microenvironment (TME) after LNP-B treatment ($n = 5$). (A–C) Representative flow cytometry plots of immunosuppressive cells including (A) MDSCs ($CD11b^+Ly6C^+$), (B) Tregs ($CD25^+Foxp3^+$), and M2 macrophages ($F4/80^+CD206^+$), and (D–F) the quantitative analysis of these immunosuppressive cells in the TME after different treatments. (G–I) Representative flow cytometry plots of anti-tumor immune cells including (G) $CD49b^+CD69^+$ NK cells, (H) $CD3^+CD8^+$ T cells, and (I) $CD80^+CD86^+$ DCs, and (J–L) the quantitative analysis of these anti-tumor immune cells in the TME after different treatments. Data are expressed as mean ± SD. One-way ANOVA analysis was conducted to test for differences among groups. $^*P < 0.05$; $^{**}P < 0.01$; $^{***}P < 0.001$; and ns, no difference between two groups.

resistance towards it. The reasons behind this resistance seem to be linked to two different characteristics of the tumor. Firstly, the accumulation of cells that suppress the immune system within the tumor microenvironment. Secondly, there is a decrease in the infiltration and functioning of immunocytes, which are responsible for the immune response against tumor cells[78,79]. In cancer, tumor growth is aided by M2 macrophages, which are the major leukocyte population infiltrating cancers[80]. M2 macrophages support tumor survival by suppressing the proliferation of CD8$^+$ T cells and creating a tumor-favorable microenvironment by secreting biochemical mediators that promote cancer cell survival, proliferation, and eventual metastasis[81]. The re-polarization of M2 macrophages to the M1 immunostimulatory phenotype is a widely pursued strategy for suppressing tumor growth[82]. Consequently, the immunity of TME after LNP-B treatment was analyzed. Surprisingly, compared with CDNs or PBS, LNP-B and LNP-D not only significantly reduced intratumoral immunosuppressive MDSCs and Tregs, but also significantly promoted M2-to-M1 repolarization of intratumoral macrophages which could enhance NK cells to suppress cancer[18,83] (Fig. 9A−F). Subsequently, anti-tumor immunocytes in tumors after LNP-B treatment were examined. NK cells were the first line of defense against cancer cells which could kill tumor cells directly, independently of antigen sensitization, and antibody participation, and without any MHC limitation[84]. It was found that LNP-B or LNP-D significantly increased the activated NK cells and induced robust amplification of CD8$^+$ T cells and DCs maturation in TME compared with CDNs or PBS (Fig. 9G−L). Overall, it has been demonstrated that LNP-B was capable of stimulating a strong immune response in tumors. This response includes activation of innate immune cells such as NK cells and DCs, as well as the adaptive immune cells which are involved in CD8$^+$ T. Additionally, LNP-B has been found to decrease the population of immunosuppressive cells like MDSCs, Tregs and repolarize the TAM. Collectively, these findings contribute to a transformation of the "cold" tumor environment into the "hot" tumor environment, indicating a favorable tumor immune microenvironment for anti-tumor activity.

3.10. *The safety and biocompatibility of LNP-B*

While the use of LNP-B for anti-tumor purposes has yielded promising results, there have been some fluctuations in body weight that have raised safety concerns regarding these therapeutic approaches. In order to assess the possible systemic toxicity of LNP-B treatment, H&E staining was performed on major organs including the heart, liver, spleen, lung, and kidneys. It was found that PBS, free CDNs, and LNP-B treatments did not show any significant histological damage (Fig. 10A and B). The detection results of heart injury-related indicators and kidney function-related indicators in the blood indicated that LNP-B does not induce damage to the heart and kidneys (Supporting Information Fig. S18). These results indicate the bio-safety of the LNP-B therapeutic strategy.

However, the LNP-D treatment showed significant liver damage, a large number of immune cell infiltration, and loss of liver cells (Fig. 10B). The analysis of liver function biomarkers demonstrated that LNP-B did not cause significant changes in the

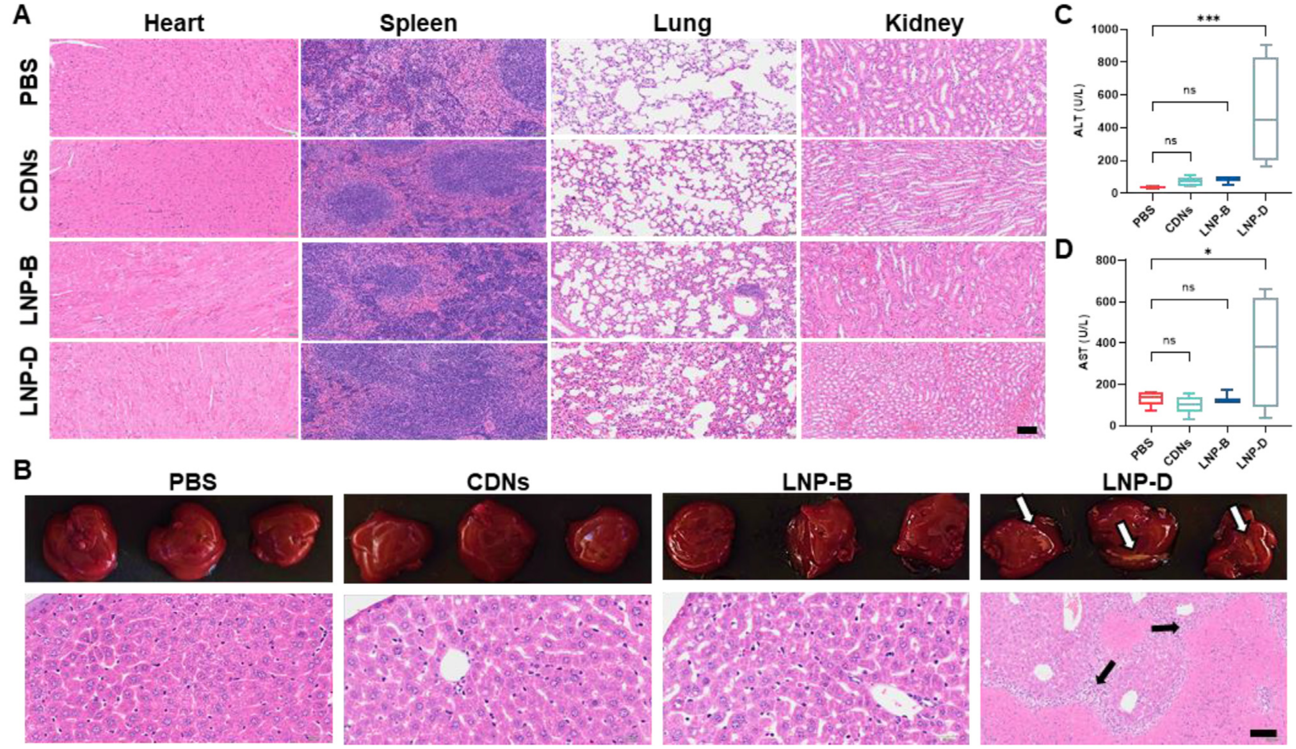

Figure 10 The safety and biocompatibility of LNP-B. (A) Representative images of H&E-stained slices of major organs including the heart, spleen, lung, and kidneys at three days after different treatments (Scale bar = 100 μm). (B) Photos of livers and representative images of H&E-stained liver slices at three days after different treatments (scale bar = 50 μm, $n = 3$). White arrow indicated liver necrosis, and black arrows indicated immune cell infiltration and loss of liver cells. (C, D) Blood biochemical indicators of (C) alanine transaminase (ALT) and (D) aspartate aminotransferase (AST) on Day 3 after different treatments ($n = 5$). Data are expressed as mean ± SD. One-way ANOVA analysis was conducted to test for differences among groups. *$P < 0.05$; ***$P < 0.001$; and ns, no difference between two groups.

activities of alanine transaminase (ALT) and aspartate aminotransferase (AST) while LNP-D induced a marked elevation in the activities of ALT and AST at three days post-treatment, compared with PBS or CDNs (Fig. 10C and D). Compared with LNP-D made from cationic DOTAP, LNP-B made from pH-sensitive polycationic DSPE-PCB$^+$ had lower toxicity to major organs. Based on the findings, it can be inferred that LNP-B exhibits potential as a safe and effective therapeutic strategy. Further studies are required to investigate the underlying mechanism behind the potential weight loss associated with LNP-B and to develop strategies aimed at minimizing its potential adverse effects. Moreover, the relationship between the structure of DSPE-PCB$^+$ and the function of LNP-B requires further research, so as to maximize the anti-tumor efficacy of CDNs.

4. Conclusions

In this study, a novel lipid nanoparticle (LNP-B) was synthesized as a nanocarrier to deliver STING agonists (CDNs) intravenously for the treatment of colorectal cancer. To effectively encapsulate negatively charged CDNs, a unique functional phospholipid called DSPE-PCB$^+$ with multiple positive charges at one end was synthesized for the preparation of LNPs. By utilizing the high-density positive charge of DSPE-PCB$^+$, the drug loading capacity of CDNs in LNPs was improved, LNP stability was enhanced, and lysosome escape of LNPs was achieved. Additionally, under acidic conditions, DSPE-PCB$^+$ underwent hydrolysis to transform into low-toxicity zwitterionic polymer-phospholipids, facilitating the acid-responsive release of CDNs from LNPs and improving LNP safety. It was found that LNP-B resulted in strong activation of DCs and repolarizing M2 macrophages. More importantly, the intravenous administration of LNP-B greatly enhanced the pharmacokinetic properties of CDNs and increased their targeted delivery to immune cells in the tumor, spleen, and TDLN. Surprisingly, a single intravenous administration of LNP-B demonstrated a significant inhibition of tumor growth, and the therapeutic window of CDNs was greatly extended. Analysis of the tumor immune microenvironment revealed that LNP-B activated immune cells at the tumor site, leading to a significant reduction in immunosuppressive cells (Tregs, MDSCs), notably increasing the anti-tumor immune cells (mature DCs, NK cells, CD8$^+$ T cells) and repolarizing TAM, resulting in a transformation of the tumor microenvironment from “cold” to “hot”. Preliminary safety evaluation indicates that LNP-B does not produce significant toxic side effects. In conclusion, our findings indicate that LNP-B has great potential in the efficient delivery of CDNs intravenously for potent tumor immunotherapy.

Acknowledgments

This work was supported by the National Science Foundation of China (8217070298, 81773283), the Guangdong Basic and Applied Basic Research Foundation (2021A1515220011, China). Thank Shiyanjia Lab (www.shiyanjia.com) for the drawing schematic illustration. We thank Shanghai Biotree Biotech Co., Ltd. for liquid chromatography-mass/mass spectrometry experiments.

Author contributions

Ying He: Conceptualization, Data curation, Formal analysis, Investigation, Methodology, Project administration, Visualization, Writing — original draft, Writing — review & editing. Ke Zheng: Conceptualization, Data curation, Formal analysis, Investigation, Methodology. Xifeng Qin: Formal analysis, Project administration, Writing — review & editing. Siyu Wang: Formal analysis, Methodology, Writing — review & editing. Xuejing Li: Formal analysis, Investigation, Methodology, Writing — review & editing. Huiwen Liu: Formal analysis, Investigation, Methodology. Mingyang Liu: Formal analysis, Investigation, Methodology, Writing — review & editing. Ruizhe Xu: Project administration, Software, Writing — review & editing. Shaojun Peng: Funding acquisition, Investigation, Methodology, Resources, Supervision, Writing — review & editing. Zhiqing Pang: Conceptualization, Data curation, Funding acquisition, Investigation, Methodology, Resources, Supervision, Visualization, Writing — review & editing.

Conflicts of interest

The authors declare no conflicts of interest.

Declaration of Generative AI and AI-assisted technologies in the writing process

During the preparation of this work the author(s) used AI to polish the language. After using this tool, the author(s) reviewed and edited the content as needed and took full responsibility for the content of the publication.

Appendix A. Supporting information

Supporting information to this article can be found online at https://doi.org/10.1016/j.apsb.2024.06.004.

References

1. Topalian SL, Hodi FS, Brahmer JR, Gettinger SN, Smith DC, McDermott DF, et al. Safety, activity, and immune correlates of anti-PD-1 antibody in cancer. *N Engl J Med* 2012;**366**:2443—54.
2. Cloughesy TF, Mochizuki AY, Orpilla JR, Hugo W, Lee AH, Davidson TB, et al. Neoadjuvant anti-PD-1 immunotherapy promotes a survival benefit with intratumoral and systemic immune responses in recurrent glioblastoma. *Nat Med* 2019;**25**:477—86.
3. Ying Z, Huang XF, Xiang X, Liu Y, Kang X, Song Y, et al. A safe and potent anti-CD19 CAR T cell therapy. *Nat Med* 2019;**25**:947—53.
4. Li J, Burgess DJ. Nanomedicine-based drug delivery towards tumor biological and immunological microenvironment. *Acta Pharm Sin B* 2020;**10**:2110—24.
5. Yu YK, Li TX, Ou MT, Luo R, Chen HZ, Ren H, et al. OX40L-expressing M1-like macrophage exosomes for cancer immunotherapy. *J Control Release* 2024;**365**:469—79.
6. Chen Z, Meng CY, Mai JH, Liu YB, Li HW, Shen HF. An mRNA vaccine elicits STING-dependent antitumor immune responses. *Acta Pharm Sin B* 2023;**13**:1274—86.
7. Li Q, Shi Z, Zhang F, Zeng W, Zhu D, Mei L. Symphony of nanomaterials and immunotherapy based on the cancer-immunity cycle. *Acta Pharm Sin B* 2022;**12**:107—34.
8. Sade-Feldman M, Jiao YXJ, Chen JH, Rooney MS, Barzily-Rokni M, Eliane JP, et al. Resistance to checkpoint blockade therapy through inactivation of antigen presentation. *Nat Commun* 2017;**8**:1136.
9. Iorgulescu JB, Braun D, Oliveira G, Keskin DB, Wu CJ. Acquired mechanisms of immune escape in cancer following immunotherapy. *Genome Med* 2018;**10**:87.
10. Fuertes MB, Kacha AK, Kline J, Woo S-R, Kranz DM, Murphy KM, et al. Host type I IFN signals are required for antitumor CD8$^+$ T cell

responses through CD8α+ dendritic cells. *J Exp Med* 2011;**208**:2005−16.

11. Gajewski TF, Corrales L. New perspectives on type I IFNs in cancer. *Cytokine Growth Factor Rev* 2015;**26**:175−8.
12. Patel SJ, Sanjana NE, Kishton RJ, Eidizadeh A, Vodnala SK, Cam M, et al. Identification of essential genes for cancer immunotherapy. *Nature* 2017;**548**:537−42.
13. Zhang H, You QD, Xu XL. Targeting stimulator of interferon genes (STING): a medicinal chemistry perspective. *J Med Chem* 2020;**63**:3785−816.
14. Ishikawa H, Barber GN. STING is an endoplasmic reticulum adaptor that facilitates innate immune signalling. *Nature* 2008;**455**:674−8.
15. Xu N, Palmer DC, Robeson AC, Shou PS, Bommiasamy H, Laurie SJ, et al. STING agonist promotes CAR T cell trafficking and in breast cancer. *J Exp Med* 2021;**218**:e20200844.
16. Liang S, Li J, Zou Z, Mao M, Ming S, Lin F, et al. Tetrahedral DNA nanostructures synergize with MnO_2 to enhance antitumor immunity *via* promoting STING activation and M1 polarization. *Acta Pharm Sin B* 2022;**12**:2494−505.
17. Zeng WF, Li ZM, Huang QL, Ding CD, Yang L, Wang WY, et al. Multifunctional mesoporous polydopamine-based systematic delivery of STING agonist for enhanced synergistic photothermal-immunotherapy. *Adv Funct Mater* 2024;**34**:e2307241.
18. Berger G, Knelson EH, Jimenez-Macias JL, Nowicki MO, Han S, Panagioti E, et al. STING activation promotes robust immune response and NK cell-mediated tumor regression in glioblastoma models. *Proc Natl Acad Sci U S A* 2022;**119**:e2111003119.
19. Chin EN, Yu C, Vartabedian VF, Jia Y, Kumar M, Gamo AM, et al. Antitumor activity of a systemic STING-activating non-nucleotide cGAMP mimetic. *Science* 2020;**369**:993−9.
20. Ramanjulu JM, Pesiridis GS, Yang J, Concha N, Singhaus R, Zhang SY, et al. Design of amidobenzimidazole STING receptor agonists with systemic activity. *Nature* 2018;**564**:439−43.
21. Meric-Bernstam F, Sweis RF, Kasper S, Hamid O, Bhatia S, Dummer R, et al. Combination of the STING agonist MIW815 (ADU-S100) and PD-1 inhibitor spartalizumab in advanced metastatic solid tumors or lymphomas: an open-label, multicenter, phase Ib study. *Clin Cancer Res* 2023;**29**:110−21.
22. Meric-Bernstam F, Sweis RF, Hodi FS, Messersmith WA, Andtbacka RHI, Ingham M, et al. Phase I dose-escalation trial of MIW815 (ADU-S100), an intratumoral STING Agonist, in patients with advanced/metastatic solid tumors or lymphomas. *Clin Cancer Res* 2022;**28**:677−88.
23. Yang K, Han W, Jiang X, Piffko A, Bugno J, Han C, et al. Zinc cyclic di-AMP nanoparticles target and suppress tumours *via* endothelial STING activation and tumour-associated macrophage reinvigoration. *Nat Nanotechnol* 2022;**17**:1322−31.
24. Song W, Song SJ, Kuang J, Yang H, Yu T, Yang F, et al. Activating innate immunity by a STING signal amplifier for local and systemic immunotherapy. *ACS Nano* 2022;**16**:15977−93.
25. Cheng N, Watkins-Schulz R, Junkins RD, David CN, Johnson BM, Montgomery SA, et al. A nanoparticle-incorporated STING activator enhances antitumor immunity in PD-L1-insensitive models of triple-negative breast cancer. *JCI Insight* 2018;**3**:e120638.
26. Wehbe M, Wang-Bishop L, Becker KW, Shae D, Baljon JJ, He X, et al. Nanoparticle delivery improves the pharmacokinetic properties of cyclic dinucleotide STING agonists to open a therapeutic window for intravenous administration. *J Control Release* 2021;**330**:1118−29.
27. Doshi AS, Cantin S, Prickett LB, Mele DA, Amiji M. Systemic nano-delivery of low-dose STING agonist targeted to $CD103^+$ dendritic cells for cancer immunotherapy. *J Control Release* 2022;**345**:721−33.
28. Dane EL, Belessiotis-Richards A, Backlund C, Wang JN, Hidaka K, Milling LE, et al. STING agonist delivery by tumour-penetrating PEG-lipid nanodiscs primes robust anticancer immunity. *Nat Mater* 2022;**21**:710−20.
29. Sahay G, Eygeris Y, Gupta M, Kim J. Chemistry of lipid nanoparticles for RNA delivery. *Acc Chem Res* 2022;**55**:2−12.
30. Sun XQ, Zhang Y, Li JQ, Park KS, Han K, Zhou XW, et al. Amplifying STING activation by cyclic dinucleotide-manganese particles for local and systemic cancer metalloimmunotherapy. *Nat Nanotechnol* 2021;**16**:1260−70.
31. Lv MZ, Chen MX, Zhang R, Zhang W, Wang CG, Zhang Y, et al. Manganese is critical for antitumor immune responses *via* cGAS−STING and improves the efficacy of clinical immunotherapy. *Cell Res* 2020;**30**:966−79.
32. Ladd J, Zhang Z, Chen S, Hower JC, Jiang S. Zwitterionic polymers exhibiting high resistance to nonspecific protein adsorption from human serum and plasma. *Biomacromolecules* 2008;**9**:1357−61.
33. Cao Z, Zhang L, Jiang S. Superhydrophilic zwitterionic polymers stabilize liposomes. *Langmuir* 2012;**28**:11625−32.
34. Shae D, Becker KW, Christov P, Yun DS, Lytton-Jean AKR, Sevimli S, et al. Endosomolytic polymersomes increase the activity of cyclic dinucleotide STING agonists to enhance cancer immunotherapy. *Nat Nanotechnol* 2019;**14**:269−78.
35. Kumar V, Kumar V, Luo J, Mahato RI. Therapeutic potential of OMe-PS-miR-29b1 for treating liver fibrosis. *Mol Ther* 2018;**26**:2798−811.
36. You Y, Liu Y, Ma C, Xu J, Xie L, Tong S, et al. Surface-tethered ROS-responsive micelle backpacks for boosting mesenchymal stem cell vitality and modulating inflammation in ischemic stroke treatment. *J Control Release* 2023;**362**:210−24.
37. Shi ZQ, Li QQ, Mei L. pH-Sensitive nanoscale materials as robust drug delivery systems for cancer therapy. *Chin Chem Lett* 2020;**31**:1345−56.
38. Liu C, Ruan S, He Y, Li X, Zhu Y, Wang H, et al. Broad-spectrum and powerful neutralization of bacterial toxins by erythroliposomes with the help of macrophage uptake and degradation. *Acta Pharm Sin B* 2022;**12**:4235−48.
39. Yuan XZ, Lu Y, Lee YW, Zhao DW. Nanoparticle-STING agonist enhances the tumoricidal effect of bone marrow-derived macrophage. In: *Winston-Salem, North Carolina: Biomedical Engineering*. Wake Forest University; 2021. Available from: https://wakespace.lib.wfu.edu/handle/10339/99076.
40. Harimoto T, Hahn J, Chen YY, Im J, Zhang J, Hou N, et al. A programmable encapsulation system improves delivery of therapeutic bacteria in mice. *Nat Biotechnol* 2022;**40**:1259−69.
41. Drevets DA, Canono BP, Campbell PA. Measurement of bacterial ingestion and killing by macrophages. *Curr Protoc Immunol* 2015;**109**:14.6.1−17.
42. Wculek SK, Cueto FJ, Mujal AM, Melero I, Krummel MF, Sancho D. Dendritic cells in cancer immunology and immunotherapy. *Nat Rev Immunol* 2020;**20**:7−24.
43. Jakubzick CV, Randolph GJ, Henson PM. Monocyte differentiation and antigen-presenting functions. *Nat Rev Immunol* 2017;**17**:349−62.
44. Dietz L, Oberlander J, Mateos-Maroto A, Schunke J, Fichter M, Kramer-Albers EM, et al. Uptake of extracellular vesicles into immune cells is enhanced by the protein corona. *J Extracell Vesicles* 2023;**12**:e12399.
45. Borkowska M, Siek M, Kolygina DV, Sobolev YI, Lach S, Kumar S, et al. Targeted crystallization of mixed-charge nanoparticles in lysosomes induces selective death of cancer cells. *Nat Nanotechnol* 2020;**15**:331−41.
46. Mishra S, Chakraborty H. Phosphatidylethanolamine and cholesterol promote hemifusion formation: a tug of war between membrane interfacial order and intrinsic negative curvature of lipids. *J Phys Chem B* 2023;**127**:7721−9.
47. Ramezanpour M, Tieleman DP. Computational insights into the role of cholesterol in inverted hexagonal phase stabilization and endosomal drug release. *Langmuir* 2022;**38**:7462−71.
48. Ho NT, Siggel M, Camacho KV, Bhaskara RM, Hicks JM, Yao YC, et al. Membrane fusion and drug delivery with carbon nanotube porins. *Proc Natl Acad Sci U S A* 2021;**118**:e2016974118.
49. Li Y, Cheng Q, Jiang Q, Huang Y, Liu H, Zhao Y, et al. Enhanced endosomal/lysosomal escape by distearoyl phosphoethanolamine-polycarboxybetaine lipid for systemic delivery of siRNA. *J Control Release* 2014;**176**:104−14.

50. Jneid B, Bochnakian A, Hoffmann C, Delisle F, Djacoto E, Sirven P, et al. Selective STING stimulation in dendritic cells primes antitumor T cell responses. *Sci Immunol* 2023;**8**:eabn6612.
51. Chiriva-Internati M, Liu Y, Weidanz JA, Grizzi F, You H, Zhou W, et al. Testing recombinant adeno-associated virus-gene loading of dendritic cells for generating potent cytotoxic T lymphocytes against a prototype self-antigen, multiple myeloma HM1.24. *Blood* 2003;**102**:3100−7.
52. Gilleron J, Querbes W, Zeigerer A, Borodovsky A, Marsico G, Schubert U, et al. Image-based analysis of lipid nanoparticle-mediated siRNA delivery, intracellular trafficking and endosomal escape. *Nat Biotechnol* 2013;**31**:638−46.
53. Cartiera MS, Johnson KM, Rajendran V, Caplan MJ, Saltzman WM. The uptake and intracellular fate of PLGA nanoparticles in epithelial cells. *Biomaterials* 2009;**30**:2790−8.
54. Wang Y, Luo J, Alu A, Han X, Wei Y, Wei X. cGAS−STING pathway in cancer biotherapy. *Mol Cancer* 2020;**19**:136.
55. Yum S, Li M, Chen ZJ. Old dogs, new trick: classic cancer therapies activate cGAS. *Cell Res* 2020;**30**:639−48.
56. Yu R, Zhu B, Chen D. Type I interferon-mediated tumor immunity and its role in immunotherapy. *Cell Mol Life Sci* 2022;**79**:191.
57. Kalliolias GD, Ivashkiv LB. TNF biology, pathogenic mechanisms and emerging therapeutic strategies. *Nat Rev Rheumatol* 2016;**12**:49−62.
58. Kursunel MA, Esendagli G. The untold story of IFN-γ in cancer biology. *Cytokine Growth Factor Rev* 2017;**35**:73−81.
59. Wang Q, Bergholz JS, Ding L, Lin Z, Kabraji SK, Hughes ME, et al. STING agonism reprograms tumor-associated macrophages and overcomes resistance to PARP inhibition in BRCA1-deficient models of breast cancer. *Nat Commun* 2022;**13**:3022.
60. Wang X, Zhang W. The Janus of Protein Corona on nanoparticles for tumor targeting, immunotherapy and diagnosis. *J Control Release* 2022;**345**:832−50.
61. Papini E, Tavano R, Mancin F. Opsonins and dysopsonins of nanoparticles: facts, concepts, and methodological guidelines. *Front Immunol* 2020;**11**:567365.
62. Dilliard SA, Cheng Q, Siegwart DJ. On the mechanism of tissue-specific mRNA delivery by selective organ targeting nanoparticles. *Proc Natl Acad Sci U S A* 2021;**118**:e2109256118.
63. Zhang P, Qiao Y, Zhu L, Qin M, Li Q, Liu C, et al. Nanoprobe based on biominerals in protein corona for dual-modality MR imaging and therapy of tumors. *ACS Nano* 2023;**17**:184−96.
64. Lim BC, McArdle HJ, Morgan EH. Transferrin-receptor interaction and iron uptake by reticulocytes of vertebrate animals—a comparative study. *J Comp Physiol B* 1987;**157**:363−71.
65. Chillakuri CR, Jones C, Mardon HJ. Heparin binding domain *in vitro* nectin is required for oligomerization and thus enhances integrin mediated cell adhesion and spreading. *FEBS Lett* 2010;**584**:3287−91.
66. Ruzha Y, Ni J, Quan Z, Li H, Qing H. Role of vitronectin and its receptors in neuronal function and neurodegenerative diseases. *Int J Mol Sci* 2022;**23**:12387.
67. Kim H, Villareal LB, Liu Z, Haneef M, Falcon DM, Martin DR, et al. Transferrin receptor-mediated iron uptake promotes colon tumorigenesis. *Adv Sci (Weinh)* 2023;**10**:e2207693.
68. Koneru T, McCord E, Pawar S, Tatiparti K, Sau S, Iyer AK. Transferrin: biology and use in receptor-targeted nanotherapy of gliomas. *ACS Omega* 2021;**6**:8727−33.
69. Brooks PC, Clark RA, Cheresh DA. Requirement of vascular integrin alpha v beta 3 for angiogenesis. *Science* 1994;**264**:569−71.
70. He X, Wang J, Tang Y, Chiang ST, Han T, Chen Q, et al. Recent advances of emerging spleen-targeting nanovaccines for immunotherapy. *Adv Healthc Mater* 2023;**12**:e2300351.
71. Cheng Q, Wei T, Farbiak L, Johnson LT, Dilliard SA, Siegwart DJ. Selective organ targeting (SORT) nanoparticles for tissue-specific mRNA delivery and CRISPR-Cas gene editing. *Nat Nanotechnol* 2020;**15**:313−20.
72. Pitt JM, Marabelle A, Eggermont A, Soria JC, Kroemer G, Zitvogel L. Targeting the tumor microenvironment: removing obstruction to anticancer immune responses and immunotherapy. *Ann Oncol* 2016;**27**:1482−92.
73. Bronte V, Pittet MJ. The spleen in local and systemic regulation of immunity. *Immunity* 2013;**39**:806−18.
74. Koukourakis MI, Giatromanolaki A. Tumor draining lymph nodes, immune response, and radiotherapy: towards a revisal of therapeutic principles. *Biochim Biophys Acta Rev Cancer* 2022;**1877**:188704.
75. Sistigu A, Yamazaki T, Vacchelli E, Chaba K, Enot DP, Adam J, et al. Cancer cell-autonomous contribution of type I interferon signaling to the efficacy of chemotherapy. *Nat Med* 2014;**20**:1301−9.
76. Zhao Z, Condomines M, van der Stegen SJC, Perna F, Kloss CC, Gunset G, et al. Structural design of engineered costimulation determines tumor rejection kinetics and persistence of CAR T Cells. *Cancer Cell* 2015;**28**:415−28.
77. Manz RA, Hauser AE, Hiepe F, Radbruch A. Maintenance of serum antibody levels. *Annu Rev Immunol* 2005;**23**:367−86.
78. Yang L, Li A, Lei Q, Zhang Y. Tumor-intrinsic signaling pathways: key roles in the regulation of the immunosuppressive tumor microenvironment. *J Hematol Oncol* 2019;**12**:125.
79. Ju H, Kim D, Oh YK. Lipid nanoparticle-mediated CRISPR/Cas9 gene editing and metabolic engineering for anticancer immunotherapy. *Asian J Pharm Sci* 2022;**17**:641−52.
80. Ugel S, De Sanctis F, Mandruzzato S, Bronte V. Tumor-induced myeloid deviation: when myeloid-derived suppressor cells meet tumor-associated macrophages. *J Clin Invest* 2015;**125**:3365−76.
81. Ostuni R, Kratochvill F, Murray PJ, Natoli G. Macrophages and cancer: from mechanisms to therapeutic implications. *Trends Immunol* 2015;**36**:229−39.
82. Amoozgar Z, Goldberg MS. Targeting myeloid cells using nanoparticles to improve cancer immunotherapy. *Adv Drug Deliv Rev* 2015;**91**:38−51.
83. Sun Y, Hu H, Liu Z, Xu J, Gao Y, Zhan X, et al. Macrophage STING signaling promotes NK cell to suppress colorectal cancer liver metastasis *via* 4-1BBL/4-1BB co-stimulation. *J Immunother Cancer* 2023;**11**:e006481.
84. Myers JA, Miller JS. Exploring the NK cell platform for cancer immunotherapy. *Nat Rev Clin Oncol* 2021;**18**:85−100.